$$\zeta_n = 8a^2n^2\left(\frac{3n}{aN_n}\right)^{\frac{1}{2}}\left\{\frac{(n-a)^{n-3}}{(n+a)^{n+3}}\left[n^2(1-2a)+\frac{2n^2+1}{3}\right]\right.$$

$$\left.+\frac{(a-b)(a+b)(nb-a)^{n-2}}{(a+1)^4(nb+a)^{n+2}}\right\}. \quad (7)$$

For the calculation of V_m, and V_{nm}, the following integrals may be useful:

$$\int_0^\infty r^a e^{-(\mu+1)r}[L_m{}^a(r)]^2 dr$$

$$=\frac{[(m+a)!]^3}{m!(\mu+1)^{a+2+2m}}F(-m, -m-a\,|\,1\,|\,\mu^2),$$

$$\int_0^\infty r^a e^{-\mu r}[L_m{}^a(r)]^2 dr$$

$$\times\left\{\int_0^r r'e^{-\mu r'}dr'+r\int_r^\infty e^{-\mu r'}dr'\right\} \quad (8)$$

$$=\frac{[(m+a)!]^3}{m!\mu^2}$$

$$\times\left\{1-\frac{1}{(\mu+1)^{a+2+2m}}F(-m, -m-a\,|\,1\,|\,\mu^2)\right\}.$$

Fine Structure of Singly Ionized Helium*†

Robert Novick, Edgar Lipworth, and Paul F. Yergin‡
Columbia Radiation Laboratory, Columbia University, New York, New York
(Received July 15, 1955)

The energy difference ($\mathcal{S}$) between the $2\,{}^2S_{\frac{1}{2}}$ and $2\,{}^2P_{\frac{1}{2}}$ states of ionized helium has been measured by a pulsed microwave method. Helium atoms are excited to the metastable $2\,{}^2S_{\frac{1}{2}}$ state of the ion by a microsecond pulse of electrons of about 250-ev energy. After bombardment and after the atoms and ions excited to nonmetastable states have decayed to their respective ground states, a pulse of microwave power is applied to induce the $2\,{}^2S_{\frac{1}{2}}-2\,{}^2P_{\frac{1}{2}}$ transition. This transition is followed immediately by spontaneous emission of a 40.8-ev photon associated with the $2\,{}^2P_{\frac{1}{2}}-1\,{}^2S_{\frac{1}{2}}$ transition. The photons are observed by counting photoelectrons with high-speed counters gated on synchronously with the pulses of microwave power. Two different levels of rf power are used alternately to provide a means of normalizing the data for variations in the population of the $2\,{}^2S_{\frac{1}{2}}$ state.

The present value of $\mathcal{S}$ for He$^+$ is 14 043±13 Mc/sec. The stated uncertainty is equal to three times the standard deviation plus an estimated 3 Mc/sec for the uncertainty in the corrections for systematic effects. This result, consistent with previous results, is in agreement with the best available theoretical value of 14 043.2±3.0 Mc/sec.

A. INTRODUCTION

THE energy difference ($\mathcal{S}$) between the $2\,{}^2S_{\frac{1}{2}}$ and $2\,{}^2P_{\frac{1}{2}}$ states of hydrogen and singly ionized helium is of purely radiative origin. It therefore provides a sensitive test of the theoretical predictions of quantum electrodynamics. Since the nuclear charge of ionized helium is twice that of hydrogen, the relativistic terms in the theory of the radiative shift are of greater importance in helium than they are in hydrogen. Thus the ionized helium spectrum provides a more critical test of these terms than does the hydrogen spectrum. In the present formulation of quantum electrodynamics, the radiative corrections to the energy levels of hydrogenic atoms are obtained as a double power series expansion

in the parameters α and αZ, where α is the fine structure constant and Z is the nuclear charge. A number of these terms has been computed and found to give an excellent, but not perfect, account of the observed value of $\mathcal{S}$ in hydrogen. The 0.65-Mc/sec difference between the observed value of the shift in hydrogen (1057.77 Mc/sec) (H V, p. 104)[1] and the theoretical value (1057.12 Mc/sec)[2] is six times the experimental uncertainty. If this difference arises because of a missing or incomplete term in the theory, then a sufficiently precise measure-

[1] The series of papers on the hydrogen experiments will be referred to as H I, H II, H III, H IV, H V, and H VI. These are: H I, W. E. Lamb, Jr., and R. C. Retherford, Phys. Rev. 79, 549 (1950). H II, W. E. Lamb, Jr., and R. C. Retherford, Phys. Rev. 81, 222 (1951). H III, W. E. Lamb, Jr., Phys. Rev. 85, 259 (1952). H IV, W. E. Lamb, Jr., and R. C. Retherford, Phys. Rev. 86, 1014 (1952). H V, Triebwasser, Dayhoff, and Lamb, Phys. Rev. 89, 98 (1953). H VI, Dayhoff, Triebwasser, and Lamb, Phys. Rev. 89, 106 (1953).
[2] E. E. Salpeter, Phys. Rev. 89, 92 (1953). The 0.07 Mc/sec difference between the theoretical value of S_H as given by Salpeter and as given in the present paper results from the inclusion, in the present value, of the reduced mass correction to the second order magnetic moment term (see Table V).

ment of S in He^+ will indicate the Z dependence of the term and thereby give a clue to its nature.

In 1950, Lamb and Skinner[3] made the first high-resolution measurement of S for singly ionized helium. They obtained a value of $14\,020\pm100$ Mc/sec. Since neither their method nor their apparatus was suited for very precise measurements, a new apparatus was constructed and a new method devised for a redetermination of S in He^+. In 1953, Yergin et al.[4] obtained a preliminary value of $14\,020\pm60$ Mc/sec with their new apparatus. At the time, accuracy was limited by a poor signal-to-noise ratio and by lack of a detailed theory of the line shape. Such a theory is necessary, since the natural width of the observed resonance is about 1600 Mc/sec. To obtain a result for He^+ with a fractional uncertainty which is no greater than the present fractional discrepancy between the observed and theoretical value of S in hydrogen, it is necessary to make a meaningful determination of the center of the observed line to within 1% or less of the line width. This requires a full understanding of the various systematic effects that may distort and shift the resonance curve. Subsequent to Yergin's work, the signal-to-noise ratio has been increased tenfold by an improvement of the detection efficiency. In addition, a careful study has been made of the various phenomena that determine the shape of the resonance curve. As a result of this study, a number of corrections to the observed resonance center have been discovered and evaluated. About one-fourth of the uncertainty in the results of the present experiment arises from the estimated uncertainties in these corrections; the remainder of the uncertainty is of a statistical nature.

B. METHOD

The atomic beam method developed by Lamb and Retherford (H I, p. 552) for the measurement of S in the hydrogens is not applicable to singly ionized helium because the particles are charged. In the method adopted for thi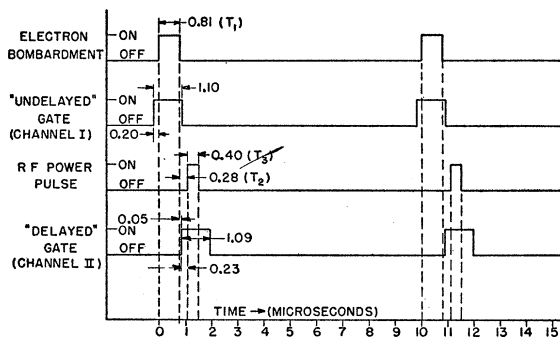s experiment, an atmosphere of helium gas at low pressure is bombarded with electrons for a period of about one microsecond (see Fig. 1). After the bombardment, there is a waiting period of about one-quarter microsecond, during which all of the ions and atoms excited to shortlived states decay to their respective ground states. Thus, at the end of the waiting period, the bombarded cloud contains ions in the ground state and the metastable $2\,{}^2S_{\frac{1}{2}}$ state,[5] as well as the two metastable atomic states (see Fig. 2). After the waiting period, an rf power source and a photomultiplier and counting channel are gated on for a period of about one microsecond. The rf electric field induces transitions from the metastable $2\,{}^2S_{\frac{1}{2}}$ state to the $2\,{}^2P_{\frac{1}{2}}$ state; the $2\,{}^2P_{\frac{1}{2}}$ state decays with a lifetime of 10^{-10} second to the ground state of the ion with the emission of $\lambda303.8$ A photon. This decay photon is detected and recorded by the photomultiplier tube and counting channel.

The above cycle of events is repeated at a rate of 10^5 cycles per second. The ions and metastable atoms diffuse to the walls of the apparatus during the eight-microsecond interval between the end of each rf pulse and the beginning of the next bombardment pulse. In addition to the "delayed" counting channel, described above, there is also an "undelayed" counting channel which is turned on in coincidence with the bombarding pulse. The undelayed count provides a convenient reference signal for normalizing the delayed count. This normalization procedure greatly reduces the effects of changes in detection efficiency, helium pressure, bombarding current, and counting time and thereby substantially improves the quality of the rf quenching data. Hereafter, the undelayed and delayed counting channels will be referred to as channel I and channel II respectively.

FIG. 1. Pulse-timing sequence.

[3] W. E. Lamb, Jr., and M. Skinner, Phys. Rev. 78, 539 (1950). This paper will be referred to hereafter as He I.
[4] Yergin, Lamb, Lipworth, and Novick, Phys. Rev. 90, 377(A) (1953).
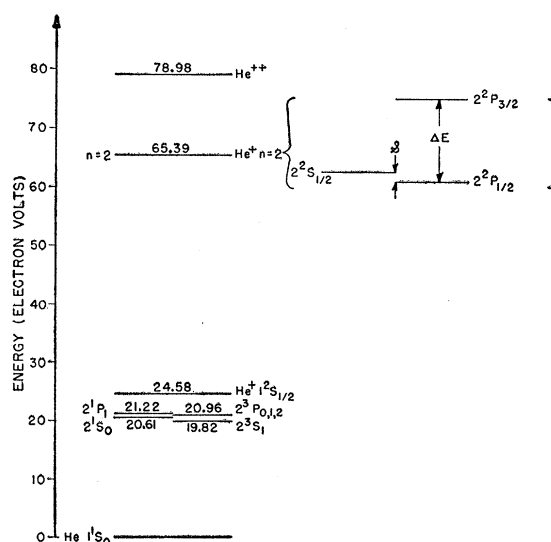

FIG. 2. Energy levels of helium.

[5] The metastability of the $2\,{}^2S_{\frac{1}{2}}$ state is discussed in Sec. E1a.
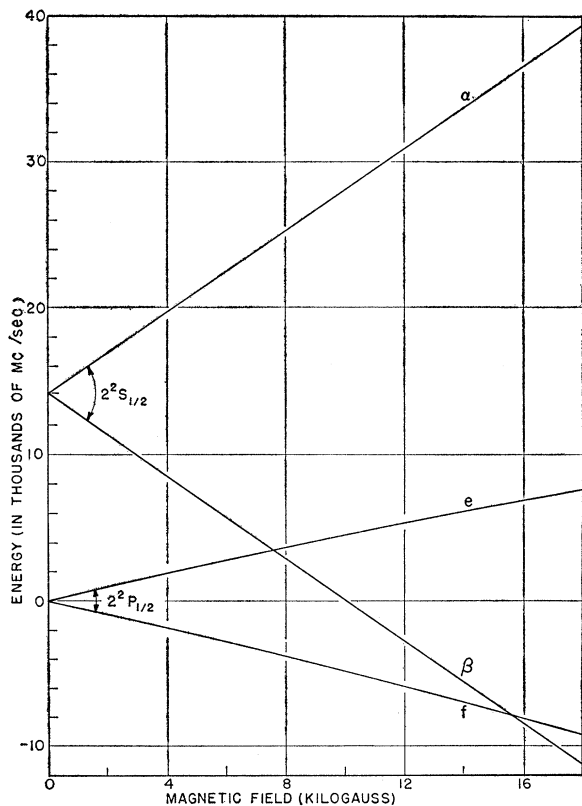
FIG. 3. Zeeman splitting of the $2\,^2S_{\frac{1}{2}}$ and $2\,^2P_{\frac{1}{2}}$ states.

FIG. 4. Zeeman transition frequencies as a function of the magnetic field.

The experiment is performed in a magnetic field primarily in order to make use of the Zeeman effect to obtain resonance between the transition frequency and a fixed frequency microwave oscillator (see Fig. 3 and Fig. 4). The alternative procedure of using a variable frequency oscillator would require the maintenance of power constant to within a fraction of one percent as the oscillator is tuned over a 10% band. Such performance would be difficult to achieve with available microwave techniques.

Resonance data are obtained in the following manner: At selected magnetic field values, three sets of channel I and channel II counts are obtained. The first set is taken with high enough rf power to quench essentially all of the metastable ions during the rf pulse. This provides a measure of the number of metastables formed at the chosen field. The second set is taken with a sufficiently low rf power, so that no more than 30% of the metastables are quenched at the peak of the resonance. This provides the basic resonance data. The third set is taken with zero rf power. This provides a measure of the background to be subtracted from each of the first two observations. Each of the channel II counts is divided by the corresponding channel I count to reduce the effect of changes in the parameters listed above. The percent rf quenching (f)
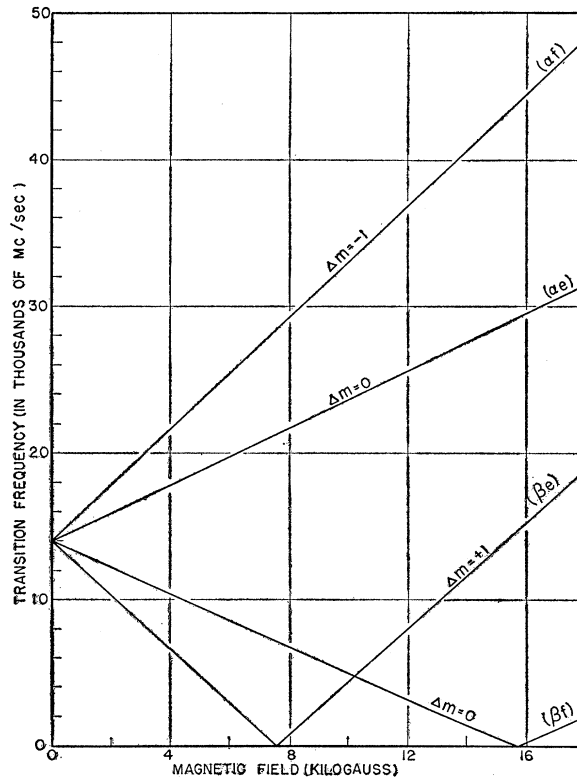
at each field value is obtained from the relation

$$f = 100(l-b)/(h-b), \qquad (1)$$

where h, l, and b are the normalized channel II counts with high, low, and zero rf power (see Table I). The values of f, so obtained form a resonance curve. The value of S is readily computed from the observed center of the resonance curve and the known oscillator frequency.

The present pulsing and waiting method has an advantage over the simultaneous bombardment and observation method of Lamb and Skinner (He I, p. 540), in that the large background arising from the shortlived ionic and atomic levels has been eliminated. This has led to a thirty-fold improvement in the signal-to-background ratio. The background from the atomic states is additionally suppressed, as in the Lamb-Skinner experiment (He I, p. 543), by resonant scattering from normal helium atoms in the path between the bombardment chamber and the detector.

The background from the short-lived atomic and ionic states may also be reduced by combining the Lamb-Skinner method with a modulated rf oscillator and a lock-in type rectifier in the output of the photodetector. With comparable observation time, the lock-in scheme should yield about the same signal-to-noise ratio as the pulse method (about 300 to 1 for a five-
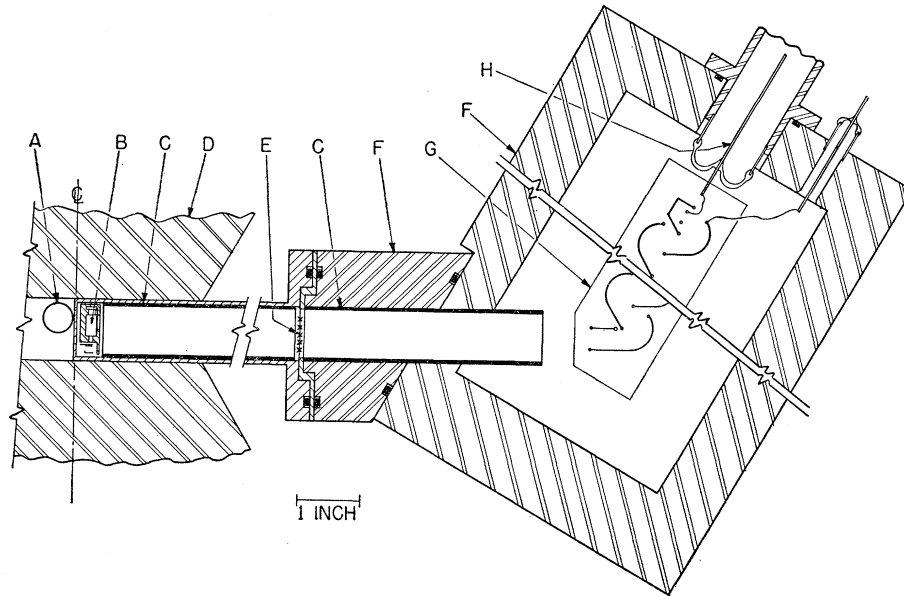
FIG. 5. Cross section of the main apparatus. A—Proton nuclear magnetic resonance probe. B—Interaction region. C—Light pipe. D—Magnet. E—Formvar film. F—Magnetic shield for the Allen tube. G—Allen type photomultiplier tube. H—Detector output connection.

minute observation time). This method has the advantage of simplicity in equipment. On the other hand, it does not have the flexibility of the pulse method and requires a resonant interaction cavity to attain a large enough rf electric field for quenching purposes with existing microwave CW sources.

C. APPARATUS

A cross section of the main apparatus is shown in Fig. 5. The essential parts are: (1) the interaction
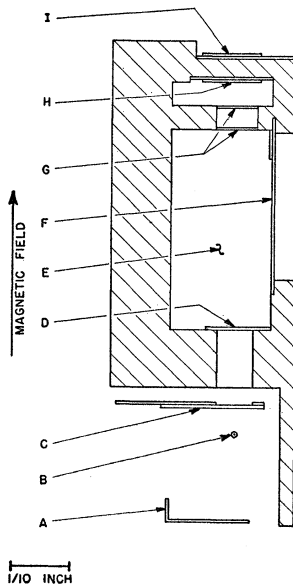

FIG. 6. Cross section of the interaction region. A—Filament shield. B—Filament. C—Control grid. D—Grid. E—Interaction space. F—Photon grid. G—Double grid. H—Electron collector. I—Electrical connection to collector.

space, (2) the detector (light pipe, Formvar film, and Allen tube), (3) the magnet, and (4) the nuclear absorption magnetometer probe. Each of these parts and their associated electronic equipment will be described in detail.

1. Interaction Space

A cross section of the interaction space is shown in Fig. 6. The body of the interaction space consists of a piece of modified K-band wave guide $(0.170 \times 0.340$ inch, inside dimensions). Attached to the wave guide are an electron gun, an electron beam collector system and a viewing grid to permit the $2\,^2P_{\frac{1}{2}}-1\,^2S_{\frac{1}{2}}$ decay photons to enter the detector. The electrical connections to the interaction space are shown in Fig. 7. The electron beam bombarding energy is determined by the steady voltage applied between the filament and the interaction space.

A hot tungsten filament 0.010 in. in diameter and 1.040 in. long serves as the electron gun cathode. The filament is heated by passing approximately 6 amp of 100 kc/sec alternating current through it. The use of the rf heating eleiminates the annoying filament-bending associated with dc heating, the vibration associated with low-frequency heating, thereby preventing possible line shape distortion resulting from displacement of the electron beam in the interaction space as the magnetic field is varied.

The filament is operated in the temperature-limited region. Thus the bombarding current may be controlled independently of the bombarding voltage and control grid bias. The heating current, and consequently the emission current, may be adjusted by varying the plate voltage of the rf filament supply oscillator.

The bombarding current is stable to better than 1% over a five-minute period. The effect of fluctuations in

the bombarding current is greatly reduced by the normalization procedure.

A control grid is located between the filament and the electron beam entrance grid at the bottom of the interaction space. The control grid is used to turn the electron beam on and off. Normally the grid is held 50 volts negative with respect to the filament. This voltage is sufficient to cut the bombarding current off completely. During bombardment the grid is pulsed to 25 volts positive, to insure that a saturation current is drawn from the cathode. No attempt is made to use electrostatic focusing, since the entire electron gun is immersed in a strong magnetic field (about 7600 gauss).

After traversing the interaction region, the electrons pass through a double grid system and then to a collector plate which is maintained at a positive potential of 225 volts. This positive collector bias prevents secondary electrons from entering the interaction region. The double grid in front of the collector prevents the electron collector field from fringing into the interaction region. Thus, except for space charge effects and possible stray fields arising from contamination, the interaction region is free of electric fields.

The shield underneath the filament is maintained at cathode potential and serves to prevent bombardment of the vacuum envelope. The control grid pulser has been designed to insure precise timing of the bombardment pulse. The pulse duration is constant to 0.1% over a period of several hours; the effective switching time is estimated to be less than 0.05 microsecond.

2. Detector

The detector consists of an eleven-stage Allen type electron multiplier tube[6] which responds to $\lambda 303.8$ A photons from the $2\,^2P_{\frac{1}{2}}-1\,^2S_{\frac{1}{2}}$ transition in the ion. Since the Allen tube must be placed outside the magnetic field, it subtends a small solid angle at the interaction space. The effective solid angle has been increased by installing a gold light pipe[7,8] between the interaction space and the Allen tube cathode. On the basis of the published data on the reflectivity of gold,[9] the light pipe was estimated to increase the effective solid angle by a factor of eighteen. After nearly one year's use, the light pipe "gain" was observed to be approximately twelve.

The Allen tube is provided with a platinum photocathode in order to reduce its sensitivity to soft photons from the electron gun filament and to reduce the thermionic background count of the multiplier. The stray magnetic field in the neighborhood of the Allen tube was reduced from about 100 gauss to less than 2 gauss

[6] J. S. Allen, Rev. Sci. Instr. **18**, 739 (1947).
[7] The light pipe consisted of a glass tube coated internally with a gold reflecting film.
[8] F. P. Bundy and H. M. Strong, J. Opt. Soc. Am. **39**, 393 (1949).
[9] H. M. O'Bryan, Phys. Rev. **38**, 32 (1931).

TABLE I. Definition of notation.

	Counts in	
Experimental condition	Channel I	Channel II
High rf power	U_h	D_h
Low rf power	U_l	D_l
rf off	U_b	D_b
Bombardment off (detector background)[a]	U_d	D_d
Counts corrected for detector background		
High rf power	$U_h'=U_h-U_d$	$H=D_h-D_d$
Low rf power	$U_l'=U_l-U_d$	$L=D_l-D_d$
rf off	$U_b'=U_b-U_d$	$B=D_b-D_d$
Normalized signals		
High-power rf signal	$=h=H/U_h'$	
Low-power rf signal	$=l=L/U_l'$	
Delayed background signal	$=b=B/U_b'$	
rf *quenching*		
High-power rf quenching	$=\phi_h=h-b$	
Low-power rf quenching	$=\phi_l=l-b$	
Percent rf quenching	$=f=100\times\phi_l/\phi_h$	

[a] Aside from the differences arising from the different observation times the channel I and channel II detector background signals are identical.

by placing a one-inch-thick soft iron shield around the tube.

A thin Formvar film is located between the multiplier and the interaction space in order to prevent metastable helium atoms from reaching the photocathode and thereby producing a large background signal.[10] This film also prevents the flow of normal helium atoms into the multiplier chamber. As a precaution against rupture, the film was mounted on a flat 150-mesh nickel grid. With this mounting the helium pressure in the multiplier is about one hundredth of the pressure in the interaction region. The thickness of the film is estimated to be about 500 A. By comparing its performance with that of a collodion film of known transmission,[11] the $\lambda 303.8$ A transmission of the film has been estimated to be about 25%. Formvar was used in preference to collodion because of its greater mechanical strength.

The long column of helium in the section of the light pipe between the interaction space and the Formvar film serves to reduce by resonant scattering[12] the signal from the excited states of atomic helium (He I, p. 550).

3. Counting System

A block diagram of the counting system is shown in Fig. 8. The two discriminator circuits are used in
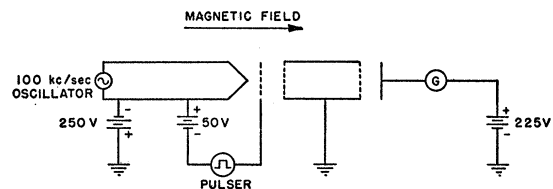
FIG. 7. Electron bombarder potentials.

[10] R. Dorrstein, Physica **9**, 433 and 447 (1942).
[11] H. M. O'Bryan, J. Opt. Soc. Am. **22**, 739 (1932).
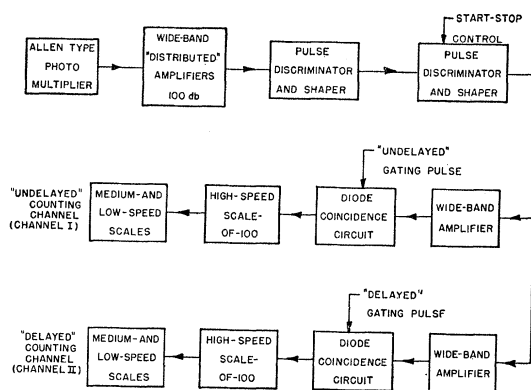[12] T. Holstein, Phys. Rev. **72**, 1212 (1947).

FIG. 8. Block diagram of the detector circuit and counting channels.

cascade in order to increase the uniformity of the signal pulses. As in the case of the gun pulse, the gate pulse duration is stable to 0.1% over a period of several hours.

The dead time for the entire detection and counting system is 0.16 microsecond. The entire counting process can be started and stopped by switching the discrimination level in the second pulse-height discriminator. The normalization procedure eliminates the effects of changes in the counting time.

The gain and band width of the amplifier chain are such that the Johnson noise and tube noise in the first amplifier are not quite large enough to trigger the first pulse-height discriminator. The total detector background signal is about 2.4 counts per second (gated). The gain of the amplifier chain is continuously monitored by a noise voltmeter connected to the grid of the first pulse-height discriminator.

4. Magnetic Field

The magnetic field is produced by an electromagnet with pole pieces $6\frac{3}{4}$ in. in diameter, tapered to 4 in. in diameter, with a gap length of 1 in. The magnet current is supplied by a motor generator set. The current is regulated by the same regulator used by Lamb and Retherford in the hydrogen experiment. (H II, p. 224.) This circuit holds the magnet field current steady to about one part in ten thousand.

The magnetic field is measured with a Pound-type proton resonance absorption apparatus.[13] The water sample and interaction region are symmetrically located about the center of the magnet. In order to facilitate the field measurements, magnetic field values are selected so that the frequency of the proton resonance occurs at integral multiples of 100 kc/sec. The width of the proton resonance is about one gauss at the base of the resonance. The field is generally stable to plus or minus one quarter of the proton line width. The uncertainty in the field measurement has been estimated to be plus or minus one gauss.

[13] R. V. Pound and W. D. Knight, Rev. Sci. Instr. 21, 219 (1950).

5. Radio-Frequency Equipment

A block diagram of the radio-frequency apparatus is shown in Fig. 9. The source of the rf power is a Raytheon type QK 289 klystron. About 250 milliwatts peak power is obtained by pulsing the klystron beam voltage to 4.5 kv. This power is barely sufficient for the purposes of the high-power rf-quenching measurement, although it is several times the rated power of the tube. The power entering the interaction region is reduced by a factor of ten for the low-power quenching measurement by inserting the attenuator. The wave-guide gate switch cuts off the power for the rf off observation.

The rf components between the interaction region and the bolometer were designed in such a way as to maintain a stable and reproducible relation between the rf field in the interaction space and the power absorbed by the bolometer.

The rf power is measured with a Polytechnic Research and Development model 618 bolometer and a model 650-A bolometer bridge. The sensitivity of the bolometer is adjusted between two fixed levels for the high power and low power measurements by manipulating the two-way rotary switch. In the high-power position, an attenuator is placed between the interaction region and the bolometer; in the low-power position, the power enters the bolometer directly from the interaction region. The power level is generally stable to a fraction of 1%.

A small fraction of the klystron power is fed into an rf envelope viewer and an rf spectrum analyzer. The shapes of the envelope and the spectrum are continuously monitored during each observation. The spectrum analyzer is also used for measuring the klystron frequency. This is accomplished by superimposing a pip
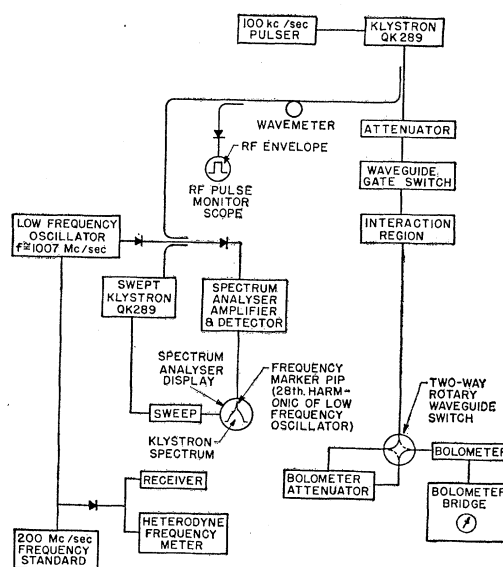

FIG. 9. Block diagram of the rf apparatus.

from the 28th harmonic of a low-frequency CW oscillator on the klystron spectrum. The frequency of the CW oscillator is determined by standard heterodyne methods. The width of the rf spectrum is close to the theoretical value of 5 Mc/sec for a 0.4-microsecond pulse. The klystron frequency is stable to plus or minus one quarter of the spectrum width. The uncertainty in the klystron frequency is estimated to be ±2.0 Mc/sec.

As an additional check on the magnetic field and klystron frequency, the electron cyclotron resonance was observed in the interaction region. Within the stated precision of the field and frequency measurements, the resonance occurred at the theoretical value

$$f_0 = eH/2\pi mc, \tag{2}$$

where f_0 is the resonant frequency, H is the magnetic field, e is the electronic charge, m is the mass of the electron and c is the velocity of light. The electron cyclotron resonance manifests itself as a large increase in the channel II high-power rf signal (h) as stray electrons are accelerated, by the resonant rf field, to the optical excitation energy of helium.

6. Timing Circuits

The various gates and pulses are controlled by a timing circuit which generates triggering impulses properly spaced in time (see Fig. 10). A 100-kc/sec sine wave from a frequency standard establishes the repetition rate of the timing cycle. The 100-kc/sec signal is squared and differentiated, and the resulting pulses drive pulse-sharpening circuits which feed two lumped constant delay lines. The trigger pulses are picked off the delay lines at times adjustable in steps of 0.1 microsecond. Four different independently adjustable trigger outputs are available. The trigger pulses from the delay lines drive sharpening circuits which reform the pulses which have been somewhat distorted by their passage through the lines. The relative timing of the various pulses is monitored continuously on an oscilloscope.

D. OPERATING CHARACTERISTICS

A careful study has been made of the operating characteristics of the apparatus. A few of the more important results of this study are presented below.

1. Signal Strength

The estimated number of high-power rf induced counts per bombardment pulse is given by

$$N = \tfrac{1}{2}\sigma^+(2S)\frac{I}{e}Ln^0T_1\eta_{PG}\eta_F\eta_{PE}C\frac{\omega}{4\pi}G, \tag{3}$$

where $\sigma^+(2S)$ is the cross section for the excitation to the $2\,^2S_{\frac{1}{2}}$ state of the ion by 250 volt electrons, I is the
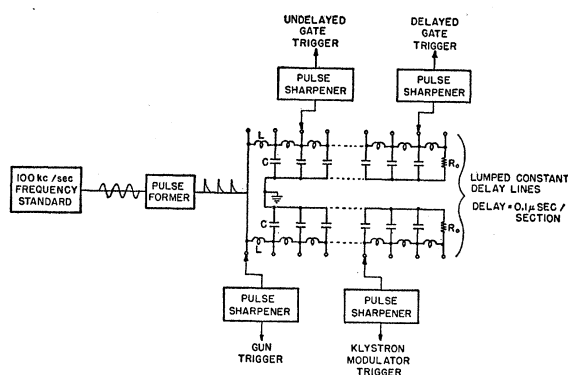

FIG. 10. Pulse-timing circuits.

bombarding current, e is the electronic charge, L is the length of the electron beam exposed to the detector, n^0 is the density of helium atoms in the interaction space, T_1 is the length of the bombarding pulse, η_F is the transmission of the Formvar film and support grid, η_{PE} is the photoelectric yield of the photocathode, η_{PG} is the transmission of the photon grid, ω is the solid angle subtended by the photocathode at the interaction space, G is the light pipe "gain" and C is the fraction of photoelectrons that are recorded by the scalers.

Lamb and Skinner (He I, p. 548) have estimated $\sigma^+(2s)$ to be

$$\sigma^+(2s) = 0.37 \times 10^{-2}\pi a_0^2, \tag{4}$$

where a_0 is the Bohr radius. Typical values for the other parameters are: $I = 740$ microamperes, $L = 0.902$ centimeter, $n^0 = 0.746 \times 10^{14}$ atoms per cm^3, $T_1 = 0.81$ microsecond, $\eta_{PG} = \frac{1}{2}$, $\eta_F = \frac{1}{4} \times \frac{1}{2} = \frac{1}{8}$ [$\frac{1}{4}$ for the film (see above) and $\frac{1}{2}$ for the grid], $\eta_{PE} = 0.05$ (Walker and Wainfan[14]) $C = \frac{1}{2}$ (see below), $\omega = 8.4 \times 10^{-5}$, and $G = 18$ (see above). Using these values, a value for N of 0.099 rf induced counts per bombardment is calculated. The observed value for N is 0.024 rf induced counts per bombardment. Thus the observed signal is about one-fourth of the estimated signal. This difference is well within the uncertainties in the cross section, the film transmission, and the photoefficiency.

2. Noise

Ideally, the fluctuations in the rf quenching data should be only slightly greater than those imposed by the shot noise in the cathode current of the photomultiplier tube. Some difficulty was encountered in achieving this theoretical limit. A large body of the data was obtained in which the observed fluctuation level was approximately ten times the theoretical value. In obtaining these data a magnetron was used as the source of rf power and the interaction region was exposed to a relatively high density of organic vapors

---

[14] W. C. Walker and N. Wainfan, Phys. Rev. 92, 533(A) (1953), and private communication.
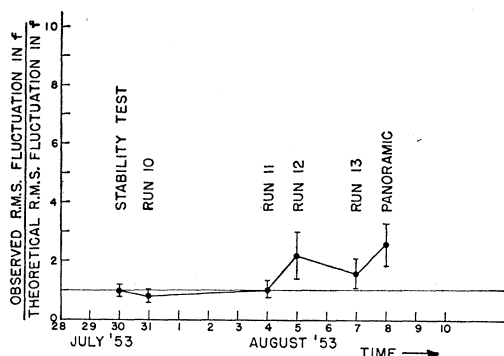
FIG. 11. Ratio of observed rms fluctuation in the rf quenching data to the theoretical fluctuation, as observed on six different occasions.

from rubber "O" rings.[15,16] Upon replacing the rubber "O" rings with Teflon "O" rings and the magnetron with a klystron, the fluctuation level in the rf quenching data dropped to the theoretical value. It is not known how much of this improvement was due to the improved rf and how much was due to the reduced contamination of the interaction region. The ratio of observed rms fluctuation in the rf quenching data to the theoretical rms fluctuation, on six different occasions, is shown in Fig. 11. The data of July 30, 1953 were taken immediately after the improvements noted above were made. These data were taken for the purpose of studying the stability of the apparatus. Since the individual signals often changed by several percent during the course of a run, the excellent agreement between the theoretical and observed fluctuations in the rf signal could not have been achieved without the normalization procedure. The source of the large fluctuations in the individual signals is believed to be either in the Allen tube or in the amplifier and counting circuits.

3. Allen Tube Characteristic

The variation of the undelayed signal (U_b'), delayed background (B) and detector background (D_d) with Allen tube voltage is shown in Fig. 12. These curves were taken with the amplifier gain and discriminator

[15] The magnetron was of low voltage, CW design, built expressly for this experiment. At the high duty cycle required in this experiment, this magnetron exhibited very severe back bombardment of the cathode with consequent instability of operation.

[16] It is believed that organic vapors condense on the walls of the interaction regions where they form charged insulating films. The electric fields from such films could easily cause significant motion of the ions in one microsecond. In support of this hypothesis, it has been observed that heavy black deposits formed on all surfaces exposed to electron bombardment. The electrical resistance of these films is in the megohm range. These films cannot be removed by extended heating in a hydrogen atmosphere at temperatures up to 1300°C. However, they can be removed by a rather short heating in air at about 700°C. From these observations it is concluded that the films are probably carbonaceous. See J. Blears, J. Sci. Instr. Suppl. No. 1, 36 (1951), and H. A. Wilcox, Phys. Rev. 74, 1743 (1948), reference 9.

setting adjusted so that the amplifier noise did not quite trigger the scalers. The rather high degree of saturation exhibited by the undelayed and delayed background counts is an indication that a large fraction of the photoelectrons is recorded by the scalers. The value of $\frac{1}{2}$, used for the counting efficiency (C) in the signal strength calculation, is based on the residual slope of these curves at the high-voltage limit. The fact that the voltage dependence of the delayed background (channel II rf off count) is very nearly the same as that of the undelayed signal shows that there is not an appreciable number of multiplier satellites having a delay of 0.05 microsecond or more.[17] It should be noted that, when the Allen tube was contaminated, there was evidence of an appreciable number of satellites at voltages as low as 2.1 kv.

The detector background count is obtained by turning off the electron gun, and then counting in the normal manner. This background is satisfactorily low and is assumed to be due to thermionic and high field emission from the photomultiplier dynodes.

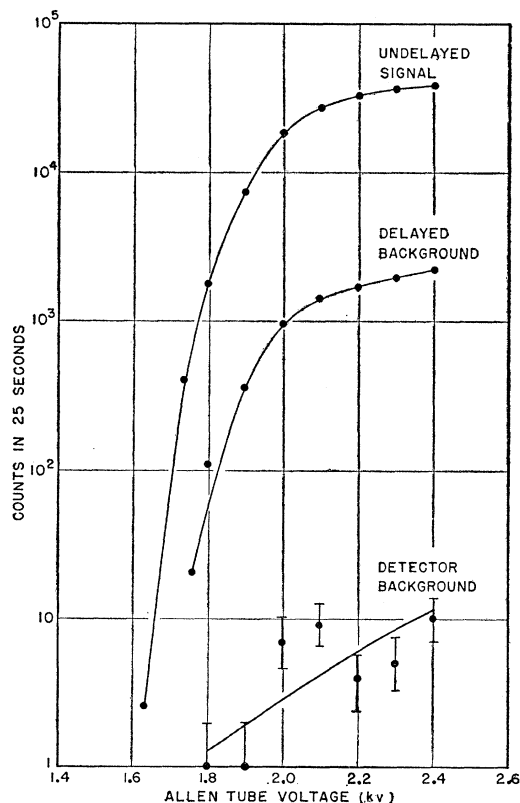FIG. 12. Variation of the undelayed (U_b'), delayed background (B) and detector background (U_d) signals with Allen tube voltage. The symbols refer to the appropriate definitions in Table I.

[17] Mueller, Best, Jackson, and Singletary, Nucleonics 10, 53 (June, 1952). We are indebted to D. W. Mueller for pointing out to us that the satellite ratio depends on the photomultiplier operating voltage.

4. Excitation Functions

Excitation curves for the undelayed signal, the delayed background, and the rf induced signal are shown in Figs. 13, 14, and 15. The observed thresholds for atomic and ionic radiation occur close to the expected values of 21 volts and 65 volts (see Fig. 2). The suppression of atomic radiation by resonance scattering and possible selective absorption in the Formvar film (He I, p. 545) are clearly evident in Figs. 13 and 14. Without this suppression the atomic radiation would be many times stronger than the ionic radiation and the threshold at 65 volts would not be visible (He I, Fig. 6, p. 544). The low voltage peak in the delayed background excitation curve is reproducible, but its origin is unknown. It is clear from Fig. 14 that most of the delayed background arises from ionic radiation. The excitation function for the metastable state of the ion (Fig. 15) does not show the sharp rise indicated in Fig. 7 of Lamb and Skinner (He I, p. 544). The reason for this is that Lamb and Skinner have plotted the ratio of the rf induced signal to background signal, and since both of these signals have very nearly the same energy dependence the resulting curve is approximately a step function. The bombarding energy used in the remainder of the experiment corresponds to the maximum of the metastable excitation function.
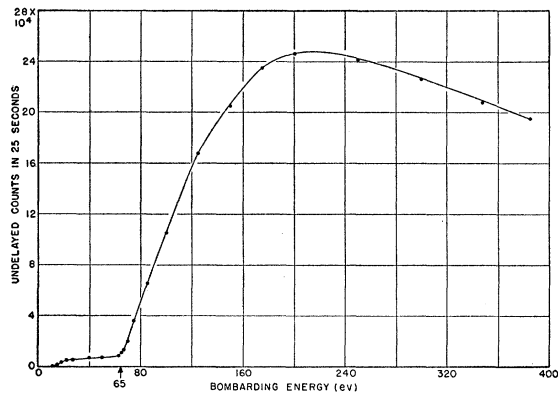

FIG. 13. Excitation curve for the undelayed signal (U_b', Table I).
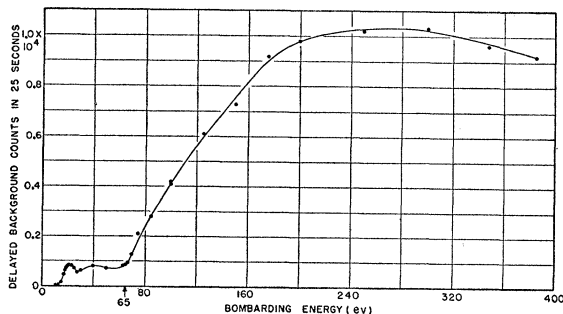

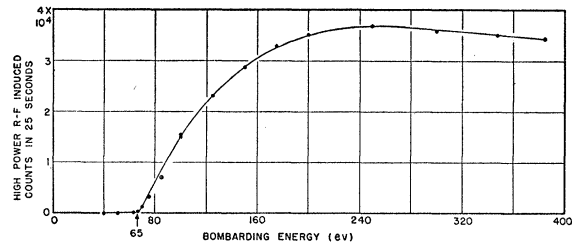FIG. 14. Excitation curve for the delayed background signal (B, Table I).

FIG. 15. Excitation curve for the high-power rf induced signal (H-B, Table I).

5. Timing Curves

The variation of the undelayed signal with channel I trigger delay setting is shown in Fig. 16. The trapezoidal shape of this curve results from the rectangular shape of the gun pulse and the gate pulse. The residual signal at large delay settings is due to the delayed background. This curve very graphically shows the reduction in background obtained with the present pulsing technique compared to the background obtained by Lamb and Skinner. The background in the latter experiment corresponds to the peak value of the undelayed signal, while the background in the present experiment corresponds to the signal at a delay setting of 2.4 μsec. Since the rf induced signal is nearly the same in the two cases, the pulsing technique results in a substantial improvement in the signal-to-background ratio. The absence of a signal at the very early delay settings shows that there are no excited particles remaining in the interaction region from bombardment to bombardment.

The variation of the delayed background and the high-power rf induced signal with the delay setting of channel II is shown in Fig. 17. The form of the delayed background curve is identical with that of the undelayed signal (see Fig. 16). The rf curve exhibits three interesting features. They are: (1) the extended flat top, (2) the nonlinear tail, and (3) the negative value at the largest delay setting. The first two features are a consequence of the fact that the curve was obtained with high rf power. Under this condition the lifetime of the metastable state is very short (roughly 0.10 microsecond in the present case), and essentially all of the rf induced counts are obtained in the early part of the rf pulse. Similar curves, taken with lower rf power and therefore a greater metastable lifetime, exhibit a shorter flat region on top. The negative value for the rf signal at the largest delay setting results from radiative collision quenching of metastable ions by normal atoms. Since this phenomenon is of only minor importance to the present experiment, though it is of some interest in its own right, a detailed discussion of the effect will be presented in a separate paper.

E. LINE SHAPE

If all of the metastable ions were exposed to the rf field for the same time (t), then aside from certain small
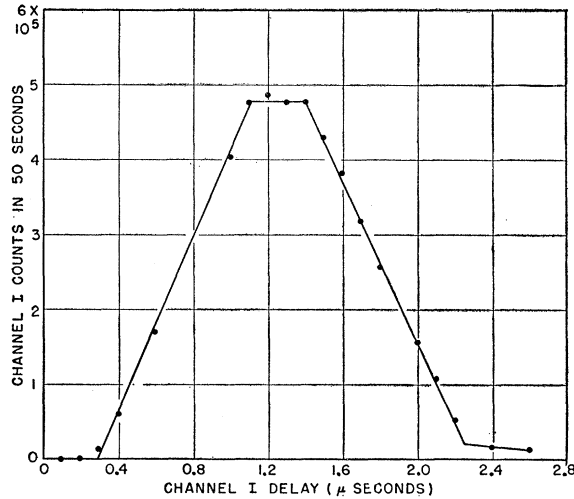
FIG. 16. Variation of the undelayed signal (U_b', Table I) with the channel I trigger delay setting.

corrections, the shape of the resulting rf quenching function would be given by

$$\phi(\mu) = N_0(1 - e^{-\mu t}), \qquad (5)$$

where N_0 is proportional to the number of metastables formed per bombardment and the transition rate μ is given by

$$\mu = \frac{2\pi S_0}{\hbar\omega} \frac{e^2}{\hbar c} \frac{\gamma\omega}{(\omega - \omega_0)^2 + (\gamma/2)^2} |\mathbf{r} \cdot \mathbf{E}|^2, \qquad (6)$$

where $1/\gamma$ is the mean life of the P state, ω_0 the resonant frequency and ω the frequency of the rf, both in radians per second, S_0 is the incident power in ergs/cm²/sec, $\mathbf{r}$ is a vector whose components are the matrix elements for the transition, and $\mathbf{E}$ is a unit vector along the
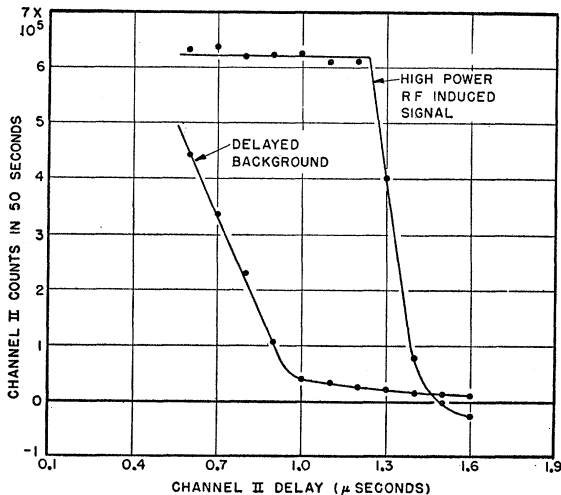

FIG. 17. Variation of the delayed background signal (B, Table I) and the high-power rf induced signal (H-B Table I) with the channel II trigger delay setting.

direction of rf polarization. Since it was desired to study the σ transition αf, ($2\,^2S_{\frac{1}{2}}$, $m = +\frac{1}{2} - 2\,^2P_{\frac{1}{2}}$, $m = -\frac{1}{2}$), the interaction space was oriented so that the rf electric field was at right angles to the magnetic field. In this case we require the matrix element of the coordinate X between the α state and the f state. This matrix element is

$$X_{\alpha f} = (\sqrt{3}/2)a_0, \qquad (7)$$

where a_0 is the Bohr radius.

In practice there is a distribution of interaction times (t). Thus, if the number of metastable ions in the interaction region decreases monotonically after the end of the gun pulse, then

$$\phi(\mu) = \mu \int_{T_2}^{T_2 + T_3} N(t)e^{-\mu(t - T_2)}dt, \qquad (8)$$

where $N(t)$ is proportional to the number of meta-stables in the interaction space at the time t (measured from the end of the gun pulse), T_2 is the delay from the end of the gun pulse to the beginning of the rf pulse and T_3 is the length of the rf pulse (Fig. 1). In deriving the above expression, the spatial variation of the transition rate μ has been approximated by a rectangular function having the same peak value and the same area as the true function (Fig. 18). In addition, the variation of the detection efficiency across the detector window has been neglected. There are several processes that contribute to the ion removal function $N(t)$. These are tabulated in Table II, together with the characteristic removal time for each process. These removal times have been computed under the assumption that each process acts independently of the others. Each of these processes will now be considered in detail.

1. Removal Process

a. Natural Decay

As a consequence of the $\Delta L = \pm 1$ selection rule, transitions from the $2\,^2S_{\frac{1}{2}}$ state to the ground state of the ion are forbidden. This accounts for the metasta-bility of the $2\,^2S_{\frac{1}{2}}$ state. The most probable decay mechanism for this state is believed to be two-quantum decay, for which the lifetime is 2.2×10^{-3} sec.[18]

b. Thermal and Recoil Velocity

The heat radiated from the electron gun filament is sufficient to raise the temperature of the interaction region to about 130°C. At this temperature the mean kinetic energy of a helium atom is 0.0521 ev.

The kinematical limits on the recoil velocity are 2.8×10^5 cm/sec in the direction of the electron flow and 0.28×10^5 cm/sec in the opposite direction. These limits are too broad to provide a useful measure of the mean recoil velocity. Lamb and Skinner used the

[18] G. Breit and E. Teller, Astrophys. J. **91**, 215 (1940).

"sudden" approximation to estimate the excitation cross section of the metastable state of the ion (He I, p. 548). This approximation is consistent with the assumption that the recoil momentum of the ion is equal to the momentum of the ejected electron in its normal state at the instant of impact. The mean value of this momentum is

$$P = Z_{eff}\alpha mc, \qquad (9)$$

where $Z_{eff} = 1.69$ is the effective value of the nuclear charge, α is the fine structure constant, m is the electronic mass, and c is the velocity of light. The corresponding recoil velocity and recoil energy are

$$v_R = 0.507 \times 10^5 \text{ cm/sec}, \quad E_R = 0.00534 \text{ ev}. \quad (10)$$

Since this energy is only about 10% of the thermal energy and since the angular distribution of the recoil velocity is not known, it is assumed that the net effect of the thermal and recoil velocities may be represented by an effective temperature of the metastable ions. This effective temperature is chosen so that the effective kinetic energy of the ions is equal to the sum of the above thermal and recoil energies. The temperature is

$$T_{eff} = 440°K. \qquad (11)$$

The corresponding rms transverse and longitudinal velocities are

$$v_T = 1.36 \times 10^5 \text{ cm/sec}, \quad v_L = 0.961 \times 10^5 \text{ cm/sec}. \quad (12)$$

Since the ions are free to move only in the direction of the magnetic field, the characteristic thermal and recoil removal time may be taken as the time for an ion, moving with a velocity of 0.96×10^5 cm/sec, to traverse the central half of the interaction region (Fig. 18).

c. Stark Quenching

In the presence of an electric field there is a Stark mixing of the $2\,^2S_{\frac{1}{2}}$ state with the shortlived $2\,^2P_{\frac{1}{2}}$ and $2\,^2P_{\frac{3}{2}}$ states. The resulting state has a lifetime somewhere between that of the S state and that of the P state. Lamb has developed a theory for this Stark quenching of the S states. The lifetime of the mixed state is given in H I, Eq. (76), p. 571.

It may be shown that for the same electric field and corresponding magnetic fields, the Stark lifetime of either of the ionized helium S states is approximately 64 times greater than the corresponding lifetime in hydrogen.

Aside from possible stray fields, the ions experience space charge and motional electric fields. The maximum values for the transverse and longitudinal space charge fields are estimated in Appendix I to be 7.9 and 2.5 v/cm respectively. The motional field is given by

$$\mathbf{E}_m = (\mathbf{V} \times \mathbf{H})/c, \qquad (13)$$

where $\mathbf{V}$ is the velocity of the ion, and $\mathbf{H}$ is the magnetic field. We may obtain an upper bound to the effective
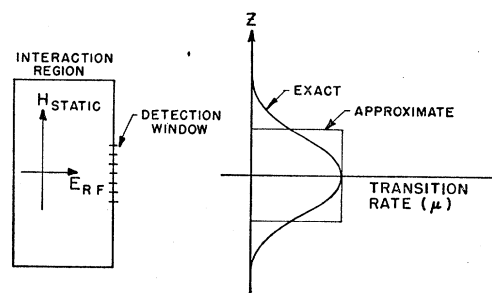

FIG. 18. Spatial variation of the rf transition rate.

electric field by adding the motional field corresponding to a velocity of 1.36×10^5 cm/sec [Eq. (12)] to the above space-charge field. The lifetimes of the α and β states resulting from this limiting field are shown as a function of the magnetic field in Fig. 19. The sharp minimum in the lifetime of the β state at a field of 7596 gauss is a result of the crossing of the β and e states at this field.

Since the Stark lifetime of the α state, as computed above, is very much greater than the other removal times (Table II), we need not seek a more refined value for the α state Stark lifetime. In the case of the β state, it appears that the Stark quenching is the dominant removal process. Fortunately, the results of the present experiment do not depend upon a precise knowledge of the lifetime of the β state. This is because the frequency of the rf field is so far removed from any of the β-state transition frequencies that, even in the high-power observation, only a negligible number of β-state ions are quenched by the rf.

d. Gas Collisions

Metastable ions are lost through encounters with normal atoms: (1) by elastic collisions which cause the ions to diffuse out of the interaction chamber and (2) by inelastic collisions which result in the quenching of the metastable ions.

Unfortunately, no estimate exists for the elastic scattering cross sections of a metastable ion by a normal atom. Hornbeck and Wannier[19] have estimated from mobility measurements that the effective cross section

TABLE II. Metastable ion loss processes.

Loss process	Characteristic loss time (μsec)
Natural decay	2200.0
Thermal and recoil velocities	4.5
Stark quenching[a]	170.0
Gas quenching	8.6
Transverse space charge motion	8.8
Longitudinal space charge motion	0.846

[a] This is for the α state. The Stark lifetime of the β state is very much less than this value.

[19] J. A. Hornbeck and G. H. Wannier, Phys. Rev. **82**, 458 (1951). J. A. Hornbeck, Phys. Rev. **84**, 615 (1951).
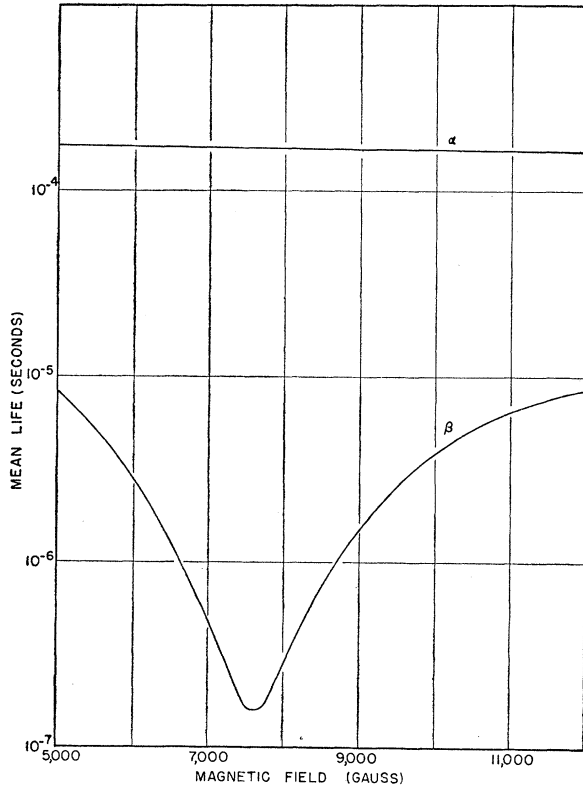
FIG. 19. Dependence of the net lifetime of the α and β states on the magnetic field.

for the collision of a normal ion with a normal atom is $61.8\pi a_0^2$. It seems reasonable to assume that the corresponding cross section for the metastable ion is of the same order or perhaps smaller than the above value. Under this assumption the elastic mean free path of a metastable ion is 2.5 cm at a gas density of 0.748×10^{14} atoms/cc (this density corresponds to the normal experimental conditions). Since the entire experiment takes place in a region having a maximum dimension of 0.5 cm, it is permissible to neglect elastic collisions in discussing the motion of the ions.

There are two classes of quenching collisions which are important in the present range of pressure and velocity. In the first, the ion returns to its ground state with its excitation energy of 40.8 ev used to ionize the helium atom with the ejection of an electron with 16.2-ev energy. In the second, the helium atom remains in its ground state but the $2\ ^2S_{\frac{1}{2}}$ ion is transferred to the nearby $2\ ^2P_{\frac{1}{2}}$ or $2\ ^2P_{\frac{3}{2}}$ states. Since the ions transferred to the P states quickly decay to the ground state, with the emission of a $\lambda303.8$ A photon, the latter process accounts for the observed radiative collision quenching of metastable ions by normal atoms (see Sec. D5). Lamb and Sternberg[20] have estimated that, at a velocity of 3×10^5 cm/sec and a gas density of 0.748×10^{14} atoms/cc, the cross sections and mean lifetimes for the

[20] W. E. Lamb, Jr., and D. Sternberg (private communication).

above processes are:

$$\sigma_e=18\pi a_0^2, \quad \tau_e=28\ \mu\text{sec},$$
$$\sigma_r=41\pi a_0^2, \quad \tau_r=12\ \mu\text{sec}, \tag{14}$$
$$\sigma_q=59\pi a_0^2, \quad \tau_q=8.6\ \mu\text{sec}.$$

where the subscript e refers to the ejection process, r to the radiative process, and q to the combined effect of both processes. The velocity used in the above calculation is believed to be representative of the collision velocity. It is the sum of the mean thermal velocity of the atoms and the mean ion velocity resulting from space charge explosion (see Appendix I).

e. Space-Charge Effects

In the absence of positive ions, the electron beam forms a potential well approximately 0.65 ev deep in the interaction region. Since the combined thermal and recoil energy of the ions is about 0.057 ev, this potential well traps the ions as they are formed. The rate of ionization is such that neutralization occurs only slightly before the end of the gun pulse; thus essentially all of the ions are trapped. Since the bombarding electrons have a velocity of 0.93×10^9 cm/sec, the density of these electrons drops to zero as soon as the electron beam is turned off by the control grid. It is assumed that the secondary electrons liberated in the gas have a velocity corresponding to the recoil momentum in Eq. (9).

$$V_s=Z_{\text{eff}}\alpha c=3.7\times10^8\ \text{cm/sec}, \tag{15}$$

where V_s is the velocity of the secondary gas electrons. Most of these electrons leave the interaction region during the bombardment pulse. Thus at the end of the gun pulse there is a pure positive ion space charge cloud in the interaction region. The dominant mode of decay of such a cloud is a Coulomb explosion along the magnetic field lines. In addition, there is a transverse cycloidal motion resulting from the combined action of the magnetic field and the transverse space charge electric field. This cycloidal motion results in a transverse shearing of the ion cloud in the direction of rf propagation.

In Appendix I a detailed estimate is made of both the Coulomb explosion and the transverse shearing of the ion cloud. It is shown that as a result of the Coulomb explosion the ion density decreases as

$$\rho(t)=\rho_0\{1/[1+(t/T)^2]\}, \tag{16}$$

where $\rho(t)$ is the ion density at the line t, measured from the end of the gun pulse; ρ_0 is the initial ion density, and the characteristic time T is 0.846 μsec for a typical set of experimental conditions. It is further shown that, for the same set of conditions and in the absence of the longitudinal Coulomb explosion, the shearing motion causes the number of ions exposed to the detector to drop to half the initial number in 8.8 μsec.

2. Theoretical Quenching Function

From the above discussion it is evident that the Coulomb explosion of the ion cloud is the dominant ion removal mechanism. Accordingly, a theory of the rf quenching function has been developed in which the motion of the ions is given by Eq. (24). This theory includes the radiative and nonradiative gas quenching discussed above. It is also possible to include Stark quenching and natural decays. However, since these are such slow processes there is little point in considering them further. The resulting rf quenching function is

$$\phi(\mu)=(\mu+\lambda_r)\phi_0 e^{-\lambda_g T_2}\int_{T_2}^{T_2+T_3} dt \frac{e^{-(\mu+\lambda_g)(t-T_2)}}{1+(t/T)^2}, \quad (17)$$

where μ is defined in Eq. (6), T is defined in Eq. (25), ϕ_0 is a normalization constant, T_2 and T_3 are defined in Fig. 1. $\lambda_r=1/\tau_r$ is the rate of radiative gas quenching
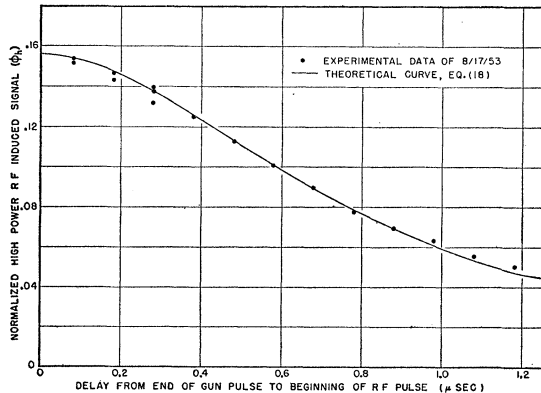

FIG. 20. Rf delay curve showing the dependence of the normalized high-power rf-induced signal (ϕ_h, Table I) on the delay between the end of the gun pulse and the beginning of the rf pulse.

and $\lambda_g=1/\tau_q$ is the total rate of gas quenching [τ_r and τ_q are given in Eq. (14)]. The quantity that is experimentally observed is the rf induced signal; by definition this is the difference between channel II count taken with and without rf. This quantity, $F(\mu)$, is related to the above quenching function by

$$F(\mu)=\phi(\mu)-\phi(0). \quad (18)$$

The percent rf quenching defined in Eq. (1) is given by

$$f=100\times\frac{F(\mu_l)}{F(\mu_h)}=100\times\frac{\phi(\mu_l)-\phi(0)}{\phi(\mu_h)-\phi(0)}, \quad (19)$$

where μ_l is the rf transition rate corresponding to the low rf power and μ_h is the same quantity with high rf power.

3. Comparison with Experiment

The above quenching theory has been tested experimentally in three different ways.

a. Delay Curves

The variation of the high-power rf-induced signal with the delay between the end of the gun pulse and the beginning of the rf pulse is shown in Fig. 20. Since this curve provides an almost direct measure of the decay of the metastable ion population, it serves as a good test of the above ion removal theory. The theoretical curve shown in Fig. 20 was obtained from Eqs. (17) and (18) by allowing the delay time (T_2) to assume appropriate values. The agreement between the observed and theoretical values is probably better than might be expected for such a rough theory. Data obtained in April, 1953, under similar conditions, showed comparable agreement. On two occasions rf delay curves were obtained with one-tenth the normal bombarding current. In such a case it is expected that the characteristic loss time would be increased by a factor of $\sqrt{10}=3.16$ [Eq. (25)], but unfortunately neither of these curves showed the expected increase. In one there was an increase of approximately a factor of 2, while in the other there was almost no increase. The former result may be consistent with the theory if thermal and recoil velocities are taken into account. The latter result is not understood. It may be the result of contamination in the interaction space, since the data were obtained after nearly three weeks of continuous running.[21] It should be noted that the precision resonance data were obtained soon after a thorough cleaning of the interaction space.

b. Quenching Curves

The variation of the rf-induced signal with rf power is shown in Fig. 21. The data obtained at magnetic field values other than the resonance value were shifted on the power scale in accordance with Eq. (6) so that
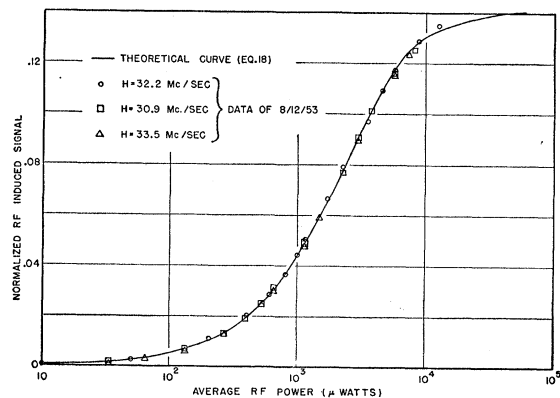

FIG. 21. Quenching curves showing the variation of the normalized rf-induced signal with rf power at three values of the magnetic field corresponding to resonance and the two working points.

---

[21] An inspection of the interaction space immediately after these data were obtained revealed a slight black deposit on the electron collector.

they could be compared with the resonance data. The agreement of the curves obtained at different field values is an indication that there are no major asymmetries in the experimental resonance curve. Unfortunately, such a test is not precise enough for the purposes of the present experiment.

The theoretical quenching function given in Eq. (18) is also shown in Fig. 21. The only adjustable parameters in the theoretical curve are the vertical and horizontal scale factors. Since the curves are plotted against the logarithm of the rf power, the horizontal scale factor does not affect the shape of the curves. The agreement between the observed and the theoretical curves is quite satisfactory.

The effective rf power in the interaction region, determined by fitting the theoretical quenching function to the observed quenching curves, is roughly 1.5 times greater than the power indicated by the bolometer. This difference can be accounted for by rf losses in the waveguide between the interaction region and the bolometer.

c. Panoramic Resonance Curves

The field dependence of the observed percent rf quenching is shown in Fig. 22, together with a theoretical curve obtained from Eq. (19). In deriving the theoretical curve, allowance was made for the field dependence of the matrix element (H III, p. 270), for the exact dependence of the transition frequency on the magnetic field (H III, p. 265), and for the width of the klystron spectrum. The transition frequency for the theoretical curve was based on the theoretical value of S (Table V). The power scale factor was adjusted for the best fit at the resonance peak. In this fitting, the ratio of the high-power to low-power transition rate was held equal to the observed ratio of high rf power to to low rf power. As in the case of the quenching curves, the agreement between the observed and theoretical curves indicates no large asymmetries in the observed resonance curve.
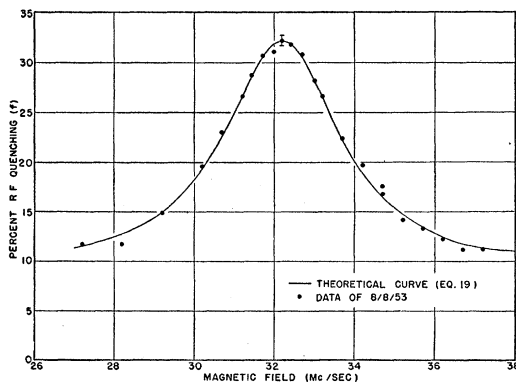
The field dependence of the high-power rf-induced signal is shown in Fig. 23. This curve shows the degree of rf saturation actually achieved in the high-power observations. The curve is quite flat in the region where the precision resonance data is obtained (30.5 to 33.5 Mc/sec). The only effect of the incomplete saturation of the high power rf quenching data is to broaden the percent rf quenching resonance curve.

Since the channel I signal is somewhat field dependent, the normalization procedure introduces a field dependent distortion into the low-power and high-power rf-induced signals. For this reason it is not feasible to compare the observed field dependence of the rf-induced signals with theoretical curves. Since this distortion affects the low-power and high-power signals in the same manner, there is no net distortion of the percent rf quenching data.

The field dependence of the delayed background signal is shown in Fig. 24. The field-dependent part of this background arises from the Stark quenching of
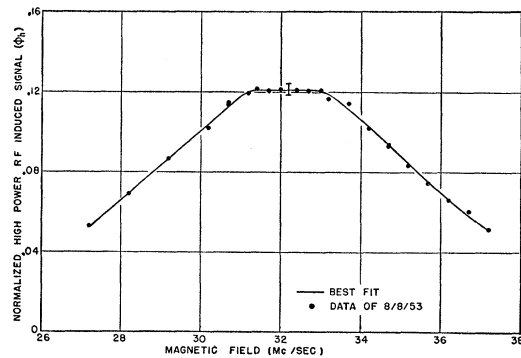
FIG. 23. High-power panoramic resonance curve showing the dependence of the normalized high-power rf-induced signal (ϕ_h, Table I) on magnetic field. The vertical bar indicates the standard deviation of each point.

metastable ions formed in the β state. Close to the βe crossing point (Fig. 19), most of these ions decay before the channel II gate is turned on and thus make only a small contribution to the delayed background; as the field is varied the Stark lifetime increases, so that more of these ions decay during the channel II gate and thereby increases the delayed background; as the field is varied still further from the crossing point, the lifetime becomes long compared with the channel II gate length and the β-state contribution to the delayed background decreases again. No quantitative theory for the field dependence of the delayed background signal was made since such a theory requires detailed knowledge of the electric fields in the interaction region as well as precise knowledge of the relative excitation and detection efficiencies of the various levels.

F. PRECISION RESONANCE DATA

The precision resonance data were obtained and treated by a method similar to that used by Lamb and

FIG. 22. Panoramic resonance curve for the αf transition showing the dependence of the percent rf quenching (f, Table I) on the magnetic field. The vertical bar indicates the standard deviation of each point.

Retherford (H IV, p. 1017). Precise data are obtained at two points on the resonance curve known as working points; these are selected to fall close to the inflection points of the curve. Somewhat less precise data are obtained at two sets of points known as slope points; each set of slope points brackets a working point. Several short observations are made close to the center of the resonance. These are used to determine the peak height of the resonance and to provide a measure of the instrumental fluctuations (Fig. 11). If the values of the rf quenching at the two working points are exactly equal, then the resonant field is equal to the mean value of the two working point fields. In general the rf quenching values at the working points are not exactly equal: in such a case it is necessary to use the observed slopes of the resonance curve to extrapolate the working point fields to values which would yield equal quenching. The resonant field (H_0) is equal to the mean value of the corrected working point fields.

$$H_0 = \tfrac{1}{2}(H_1 + H_2) - \tfrac{1}{4}(\bar{f}_1 - \bar{f}_2)\left(\frac{1}{S_1} + \frac{1}{|S_2|}\right), \quad (20)$$

where H_1 and H_2 are the working point fields, $\bar{f}_1$ and $\bar{f}_2$ are the average values of the percent rf quenching at the working points, and S_1 and S_2 are the observed slopes at H_1 and H_2, respectively.

This procedure has the advantage of being completely objective, but it has the disadvantage of not providing any measure of the asymmetries in the resonance curve. The quenching and panoramic resonance curves discussed above show that there are no major asymmetries in the resonance curve. A number of small asymmetries and resonance shifts are investigated theoretically in the next section.

Generally, each run consisted of two observations at each working point, one observation at each slope point, and six observations at the resonance peak. Each observation consisted of a high-rf power, a low-rf power and an rf-off reading. The counting time for each reading was five minutes at the working points, three minutes at the slope points, and one minute at the resonance peak. The resonance curve is traversed in a zig-zag pattern to reduce the effects of the instrumental drifts. The observations at the resonance peak were taken between alternate pairs of the other observations. The comparatively small number of observations at each field value is a result of the somewhat cumbersome field measuring and stabilizing equipment, approximately five minutes being required to set up a particular field value. Typical operating conditions for a run are: Electron bombarding energy= 250 ev; electron bombarding current= 742 μa (peak); positive grid pulse= 24 v; negative grid bias= 50 v; electron collector bias= 225 v; gun pulse length= 0.81 μsec; rf pulse length= 0.40 μsec; gate I length= 1.104 μsec; gate II length= 1.089 μsec; pulse repetition rate= 10^5 pulses/sec; helium pressure= 3.1×10^{-3} mm Hg; Allen
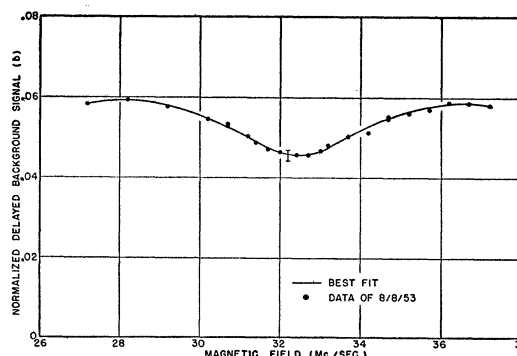

FIG. 24. Field dependence of the normalized delayed background signal (b, Table I). The vertical bar indicates the standard deviation of each point. The position of the minimum does not coincide with the position of the maximum in Fig. 22 since the klystron frequency was selected so that the resonant field for the αf transition did not correspond to the βe crossing field (Fig. 3).

tube voltage= 2.30 kv; Allen tube pressure= 1.5×10^{-6} mm Hg (N$_2$ equiv.); klystron beam voltage= 4.8 kv; klystron beam current= 38 ma (peak); high-rf power = 0.250 w (peak), and low-rf power= 0.025 w (peak).

The resonance field was selected close to the βe crossing point in order to minimize resonance distortion arising from β-state transitions. This is accomplished for the following reasons: (1) at the crossing, the β-state population is minimized due to the rapid Stark quenching (Fig. 19), (2) the βe-αf overlap is smallest at this field, and (3) the field dependence of the βe transition is symmetrical with respect to the αf resonance.

The results of the precision runs are shown in Table III. Appropriate dead time corrections have been applied to these data.[22] The theoretical quenching uncertainties listed in Table III are based on the theoretical rms uncertainty in each of the observed counts. The ratio of the observed rms fluctuation in the percent rf quenching at the resonance peak to the theoretical value for each of the precision runs is shown in Fig. 11. The approximate equality of the observed and theoretical fluctuation shows that there are no large instrumental fluctuations. A comparison of the observed and theoretical fluctuations in the working point data is less significant, since only two observations are made at each working point. The theoretical slope uncertainties listed in Table III include the effects of both the theoretical rms uncertainty in each of the observed counts and an estimated one gauss uncertainty in each of the field measurements. The observed slopes on either side of the resonance are equal to within the theoretical uncertainties in the slopes. This is taken as a further indication of a symmetrical resonance curve.

---

[22] Each run was reduced both with and without the dead time corrections. In no case did the dead time corrections change the value of S by more than 1 Mc/sec. The dead time corrections are entirely negligible for the quenching and panoramic resonance curves.

TABLE III. Summary of precision data and results.[a]

Run	Klystron frequency (Mc/sec)	Magnetic field (Mc/sec)	Total counting time (min)	No. of observations	Average fractional quenching (%)	Theor. quenching uncertainty (%)	Obs. quenching uncertainty (%)	Resonance slope (% per Mc/sec)	Theor. slope uncertainty (% per Mc/sec)	Uncorrected value of $\mathcal{S}$ (Mc/sec)	Wt.	Theor. uncertainty in $\mathcal{S}$ (Mc/sec)
10	28 196.0	30.5	3	1	22.31	0.14						
		30.7	10	2	24.294	0.073	0.27	8.80	0.51			
		30.9	3	1	25.83	0.13						
		32.0	6	6	31.496	0.097	0.078			14 038.0	1	3.8
		33.1	3	1	25.18	0.14						
		33.3	11	3	23.564	0.062	0.21	8.70	0.49			
		33.5	3	1	21.70	0.13						
11	28 350.9	30.8	3	1	24.23	0.15						
		31.0	10	2	26.380	0.074	0.033	9.70	0.52			
		31.2	3	1	28.11	0.14						
		32.3	7	7	33.846	0.090	0.095			14 046.0	1	3.8
		33.4	3	1	27.80	0.15						
		33.6	10	2	26.132	0.072	0.17	8.63	0.51			
		33.8	3	1	24.35	0.14						
12	28 294.0	30.7	3	1	21.08	0.13						
		30.9	5	1	22.65	0.10		7.33	0.45			
		31.1	3	1	24.01	0.12						
		32.2	5	5	30.472	0.093	0.20			14 058.1	½	5.0
		33.3	3	1	23.47	0.12						
		33.5	5	1	21.61	0.095		8.05	0.46			
		33.7	3	1	20.25	0.12						
13	28 305.8	30.7	3	1	23.01	0.14						
		30.9	10	2	23.945	0.076	0.14	9.65	0.49			
		31.1	3	1	26.87	0.13						
		32.2	6	6	32.460	0.094	0.15			14 042.2	1	3.8
		33.3	3	1	26.60	0.13						
		33.5	10	2	23.841	0.073	0.012	8.35	0.48			
		33.7	3	1	23.26	0.14						

$$\langle \mathcal{S} \rangle_{Av} = 14\ 044.3$$

[a] The magnetic field values are given in terms of the proton resonance absorption frequency. The uncertainties in the quenching values, the slopes, and the values of $\mathcal{S}$ are rms deviations.

The theory of the Zeeman effect, as given by Lamb (H III, p. 265), is used to determine the value of $\mathcal{S}$ from the observed value of the resonant magnetic field and the observed klystron frequency. The fine structure splitting (ΔE) for the $n=2$ states of He⁴ is given by

$$\Delta E = \frac{\alpha^2 c R_{He} Z^4}{16} \left(1 + \frac{\alpha}{\pi} - 5.946 \frac{\alpha^2}{\pi^2} + \frac{5}{8}\alpha^2 Z^2 \right),$$

where α is the fine structure constant, c is the velocity of light, R_{He} is the Rydberg constant in wave numbers for He⁴, and $Z=2$ in the nuclear charge. Using the 1953 constants of DuMond and Cohen,[23] the mass of He⁴ as determined by Mattauch and Bieri,[24] and the ratio of the proton moment (uncorrected) to the Bohr magneton as determined by Gardner,[25] the Zeeman constants appropriate to He⁴ are:

$$H_1 = 355.217 \pm 0.009 \text{ Mc/sec},$$

$$H_{1\alpha} = 355.672 \pm 0.009 \text{ Mc/sec},$$

$$H_{1a} = 355.900 \pm 0.009 \text{ Mc/sec},$$

$$T = -0.002558689 \pm 0.000000027,$$

$$f_1 = \tfrac{2}{3}\Delta E = 117\ 056.6 \pm 2.6 \text{ Mc/sec}.$$

[23] J. W. M. DuMond and E. R. Cohen, Revs. Modern Phys. 25, 691 (1953).
[24] J. Mattauch and R. Bieri, Z. Naturforsch. 9a, 303 (1954).
[25] J. H. Gardner, Phys. Rev. 83, 996 (1951).

The notation is that of Lamb (H III, p. 265), except that the unit fields are expressed in terms of the proton resonance absorption frequency. The uncertainties in the above constants produce a negligible contribution to the uncertainty in $\mathcal{S}$. The theoretical values for the rms uncertainty in $\mathcal{S}$, listed in Table III, include the effects of an estimated two megacycle per second uncertainty in the klystron frequency, an estimated one gauss uncertainty in the working point field values, the theoretical uncertainty in the working point quenching values and the theoretical uncertainty in the resonance slopes.

Run 12 has been given a weight of one-half since as a result of equipment failure only half of the normal working point data were obtained. The theoretical rms uncertainty in the weighted mean value of $\mathcal{S}(\langle \mathcal{S} \rangle_{Av})$ is

$$\Delta_T \langle \mathcal{S} \rangle_{Av} = 2.0 \text{ Mc/sec.} \tag{21}$$

The rms deviation in $\langle \mathcal{S} \rangle_{Av}$, as determined from the individual values of $\mathcal{S}$, is

$$\Delta_0 \langle \mathcal{S} \rangle_{Av} = 3.4 \text{ Mc/sec.} \tag{22}$$

The theoretical uncertainty in $\Delta_0 \langle \mathcal{S} \rangle_{Av}$ is 2.2 Mc/sec, thus the observed uncertainty in $\langle \mathcal{S} \rangle_{Av}$ is consistant with the theoretical uncertainty. The larger of the two above values of $\Delta \langle \mathcal{S} \rangle_{Av}$ is used for estimating the over-all reliability of the final result.

G. CORRECTIONS

A number of corrections to the observed value of S have been discovered and evaluated (Table IV). These corrections are discussed below. Except for the space-charge corrections, the quenching function given by Eq. (5) is used when it is necessary to consider saturation effects in the evaluation of a correction, and the interaction time (t) is taken equal to the rf pulse duration (T_3).

1. Matrix Element Variation

The form of the $2\,^2P_{\frac{1}{2}}$ wave function changes as the magnetic field is varied, and this produces a field-dependent variation of the matrix elements that appear in Eq. (6). This variation may be expressed in terms of correction factors to the matrix elements evaluated in weak field. These correction factors are given by Lamb [H III, p. 270, Eqs. (200) to (201)]. The appropriate unit field for the X that appears in these equations is listed above as H_1.

2. Zeeman Curvature

Since the relation between magnetic field and transition frequency is not quite linear (H III, p. 265), there is a small difference between the true resonant transition frequency and the value obtained in Sec. F by linear interpolation of the corrected working point fields. The Zeeman curvature correction is equal to the difference between the mean value of the transition frequencies corresponding to the corrected working point fields and the transition frequency corresponding to the mean field (H_0).

3. Overlap with Other Resonances

In addition to the desired αf transition, the rf electric field may also induce βe, αe and βf transitions (Fig. 4). The last two transitions require a component of rf electric field along the magnetic field (π polarization). If any of the undesired transitions do in fact occur, the observed resonance curve will be distorted and the value of S so obtained will be in error. The largest correction is expected to arise from overlap with the αe resonance since it is separated by only 7000 Mc/sec or roughly nine half-half widths from the αf resonance at the operating field. The βf resonance is separated by about 21 000 Mc/sec, and the βe by about 28 000 Mc/sec. The intensity of π radiation in the interaction region is believed to be less than 10% of the intensity of the desired σ radiation. Taking the relative intensity of the π radiation as 10%, and ignoring the rapid Stark quenching of the β state in the neighborhood of the αf resonance (Fig. 19), the resulting overlap corrections are $+0.20$ Mc/sec for αe overlap, -0.02 Mc/sec for βf overlap, and <0.01 Mc/sec for βe overlap. Since these are believed to be extreme upper bounds to the true corrections, the value adopted was $+0.1\pm0.01$ Mc/sec.

TABLE IV. Corrections to S in Mc/sec calculated at the working points of the resonance curve.

Matrix element variation	-1.56
Zeeman curvature	-0.25
Overlap	$+0.10\pm0.10$
Doppler effect	±0.02
Field inhomogeneity	-0.24 ± 0.60
Static stark effect	<0.01
rf stark effect	<0.01
Space-charge effects	
longitudinal	$+0.02$
transverse	$+0.21$
Total correction	-1.72 ± 0.72 Mc/sec

If the electron cyclotron resonance overlaps the desired αf resonance, there will be a distortion of the observed resonance and the value of S will be in error. It may be shown that, in the neighborhood of the αf resonance, the energy acquired by electrons from the rf field is about 2×10^{-4} ev. Since this energy is much less than the lowest excitation energy of helium, there is no electronic contribution to the rf induced signal and consequently no distortion of the αf resonance curve.

4. Doppler Effect

In Appendix I, it is shown that, as a result of the transverse space charge fields, there is a net transport of about one-fifth of the ion cloud in the direction of rf propagation. The magnitude of the resulting Doppler shift is about 0.10 Mc/sec. The sign of the shift is not known because the sign of the magnetic field was not determined. Since only one-fifth of the ions are affected the correction is taken to be ±0.02 Mc/sec.

5. Field Inhomogeneity

As a result of the spatial separation of the interaction region and the proton nuclear magnetic resonance probe, there is a slight difference between the field at the probe and the field in the interaction region. The field in the interaction region was calibrated in terms of the field at the proton probe. This was done by replacing the interaction region with a second probe and observing the difference in resonant frequencies for the two probes at a given field setting. The result of this measurement is that the field in the interaction region is higher by 0.12 ± 0.30 gauss than the field in the probe. The diamagnetic corrections to the proton field values are negligible.[26]

6. Stark Effect

For the same electric field and corresponding magnetic fields, the Stark shift in ionized helium is 1/64 of the corresponding shift in hydrogen. At a field of 11 v/cm, the Stark shift of the α state is less than 0.01 Mc/sec and is therefore negligible.

[26] W. E. Lamb, Jr., Phys. Rev. 60, 817 (1941). N. F. Ramsey, Phys. Rev. 77, 567 (1950).

7. Rf Stark Effect

The rf electric field used to produce the observed quenching also causes a small Stark displacement of the energy levels. The theory of this effect has been developed by Lamb (H III, p. 275). An rf electric field of 30 v/cm is used for the high-power rf quenching measurement. This field causes a 0.006 Mc/sec shift of the αf resonance; this displacement is entirely negligible.

8. Field Dependence of Removal Processes

a. Gas Quenching

The magnetic field dependence of the gas quenching cross section discussed in Sec. E has been evaluated by a first-order method that gives the total cross section

TABLE V. Terms contributing to the theoretical value of the separation of the $2\,^2S_{\frac{1}{2}}$ and $2\,^2P_{\frac{1}{2}}$ levels of hydrogen-like atoms, and their values in megacycles per second for singly ionized helium.

Second-order radiative shift[a-e]	
$L\left(1-3\frac{m}{M}\right)\left(2\ln\frac{1}{\alpha}+\frac{m}{M}-2\ln Z+\frac{11}{24}\right.$	
$\left.-\ln\frac{K_0(2,0)}{K_0(2,1)}\right)Z^4$	$+13\ 168.8$
Second-order vacuum polarization[a-c, e]	
$L\left(1-3\frac{m}{M}\right)(-\frac{1}{5})Z^4$	-433.9
Second-order magnetic moment[a-c, f]	
$L\left(1-2.75\frac{m}{M}\right)(\frac{1}{2})Z^4$	$+1084.7$
Second-order relativistic shift[c, g]	
$L\left(1-3\frac{m}{M}\right)(3\pi\alpha)\left(1+\frac{11}{128}-\frac{1}{2}\ln2+\frac{5}{192}\right)Z^5$	$+228.4$
Fourth-order radiative shift[b]	
$L(3\alpha/2\pi)(0.52)Z^4$	$+3.9$
Fourth-order vacuum polarization[i]	
$L(-41\alpha/54\pi)Z^4$	-3.8
Fourth-order magnetic moment[j]	
$L(-2.973\alpha/\pi)Z^4$	-15.0
Finite mass effect[k]	
$L(m/M)(5.3684-\frac{1}{2}\ln Z)Z^5$	$+3.0$
Finite size effect[c, e, l]	
$\frac{1}{24\pi}\frac{e^2}{a_0\hbar}\left(\frac{a_n}{a_0}\right)^2 Z^4$	$+7.1$
Total splitting	$\mathcal{S}=14\ 043.2\pm3.0$

Lamb constant[e]
$$L=\alpha^3 R_\infty C/3\pi=135.6388\pm0.0045\ \text{Mc/sec}$$

Excitation energies[d, e]
$$K_0(2,0)=(16.646\pm0.007)Z^2R_{He}hc$$
$$K_0(2,1)=(0.9704\pm0.0002)Z^2R_{He}hc$$

[a] See reference 27.	[g] See reference 33.
[b] See reference 28.	[h] See reference 34.
[c] See reference 29.	[i] See reference 35.
[d] See reference 30.	[j] See reference 36.
[e] See reference 31.	[k] See reference 37.
[f] See reference 32.	[l] See reference 38.

to within 10% of the value obtained by Lamb and Sternberg.[20] The cross sections given in Eq. (14) change by less than one part in 10^4 as the field is varied from one working point to the other. This effect is entirely negligible.

b. Space-Charge Effects

Since the ions move under the combined action of the space charge electric field and the applied magnetic field, it might be expected that the ion loss rate depends strongly upon the strength of the magnetic field. To first order, the ion explosion rate is independent of the magnetic field. The reason for this is simply that the explosive motion takes place along the field lines and is therefore independent of the field strength. The transverse ion less rate varies as H^{-1}, where H is the magnetic field strength. Since the transverse motion is slow, this strong field dependence produces only a small correction to $\mathcal{S}$. These qualitative arguments are supported by detailed estimates in Appendix II of the correction to $\mathcal{S}$ resulting from the field dependence of the space charge removal processes. It is shown that that for a specific space-charge model, the corrections to $\mathcal{S}$ resulting from the field dependence of the ion explosion rate and the transverse shearing motion are $+0.018$ Mc/sec and $+0.21$ Mc/sec, respectively. The model used for these estimates is admittedly rather crude; however, since the resulting corrections are so small there appears to be no need for a more refined calculation.

H. RESULTS AND DISCUSSION

The final corrected value of $\mathcal{S}$ is $14\ 043\pm13$ Mc/sec. The 13-Mc/sec uncertainty is believed to represent the limit of error; it is equal to three times the observed standard deviation of the mean value of $\mathcal{S}$ [Eq. (22)], plus an estimated 2.7 Mc/sec for the uncertainty in the corrections (0.7 Mc/sec for the uncertainty in the corrections listed in Table IV, 1.0 Mc/sec for the uncertainty in the dead time corrections, and 1.0 Mc/sec for the possible effects of the thermal and recoil velocities).

The values of the various terms that contribute to the theoretical value of $\mathcal{S}$ are listed in Table V.[27-38]

[27] N. M. Kroll and W. E. Lamb, Jr., Phys. Rev. 75, 388 (1949).
[28] J. B. French and V. F. Weisskopf, Phys. Rev. 75, 1240 (1949).
[29] Karplus, Klein, and Schwinger, Phys. Rev. 86, 288 (1952).
[30] Bethe, Brown, and Stehn, Phys. Rev. 77, 370 (1950).
[31] E. E. Salpeter, Phys. Rev. 89, 92 (1953).
[32] N. M. Kroll and W. E. Lamb, Jr., unpublished calculation of the reduced mass correction to the second-order magnetic moment contribution to $\mathcal{S}_T$.
[33] M. Baranger, Phys. Rev. 84, 866 (1951). Baranger, Bethe, and Feynman, Phys. Rev. 92, 482 (1953).
[34] Bershon, Weneser, and Kroll, Phys. Rev. 86, 596(A) (1952); Phys. Rev. 91, 1257 (1953).
[35] Baranger, Dyson, and Salpeter, Phys. Rev. 88, 680 (1952).
[36] R. Karplus and N. M. Kroll, Phys. Rev. 77, 536 (1950).
[37] E. E. Salpeter, Phys. Rev. 87, 328 (1952).
[38] Hofstadter, McAllister, and Wiener, Phys. Rev. 96, 854(A) (1954). We are indebted to Professor R. Hofstadter for communicating to us the more recent value $(1.50\pm0.25)\times10^{-13}$ cm for the rms charge radius of the α particle.

These values are based on the 1953 atomic constants of Dumond and Cohen[23] and the mass of He[4] as determined by Mattauch and Bieri.[24] The sum of these terms is $S_T = 14\,043.2 \pm 3.0$ Mc/sec.[39,40] The uncertainty in S_T arises from the uncertainties in the nuclear charge radius (2.3 Mc/sec), the fourth-order radiative shift (1.5 Mc/sec), the excitation energies (1.0 Mc/sec) and the physical constants (0.5 Mc/sec). It does not include any allowance for the contributions from terms that have not been evaluated. The essentially exact agreement of the theoretical and observed values is fortuitous.

If it is assumed that the difference between the observed and theoretical values of S for hydrogen is due to missing terms in the theory, then by comparing the present results with the hydrogen results it is possible to place limits on the charge (Z) dependence of these terms. If we let $\delta(Z)$ represent these additional theoretical terms, from the hydrogen results we have $\delta(1) = +0.65 \pm 0.26$ Mc/sec and from the present results $\delta(2) = 0 \pm 16$ Mc/sec. The uncertainties in $\delta(z)$ are obtained by adding the theoretical and experimental uncertainties. It has been suggested[33] that the hydrogen difference might be accounted for by a relativistic term of the order $Z^6 \ln\alpha Z$. If the coefficient of this term is adjusted to fit the hydrogen data then the corresponding term for helium is $\delta(2) = 36 \pm 14$ Mc/sec. This value is not consistent with the present result. Thus we conclude that the hydrogen difference is not due to a single term of order $Z^6 \ln\alpha Z$ or higher. It is possible to reconcile the hydrogen and helium results with a single term of order Z^4 or Z^5. However, the coefficient for such a term must be at least $+0.39$ Mc/sec.

ACKNOWLEDGMENTS

The authors wish to thank Professor N. M. Kroll, Professor P. Kusch, and Professor W. E. Lamb, Jr., for their continued support and guidance in this experiment. We wish to thank the members of the Columbia Radiation Laboratory staff for their wholehearted cooperation, and especially to A. H. Barrett, A. W. Costello, C. Dechert, and H. Scharfstein.

APPENDIX I. SPACE-CHARGE REMOVAL PROCESSES

For the purpose of estimating the rate of space-charge explosion, a model consisting of a uniform rectangular cloud of ions constrained to move along the magnetic field lines is considered. It is assumed that the ions are initially at rest and that the Coulomb repulsion is "turned on" at a time corresponding to the end of

the gun pulse (Fig. 25). Since an exact treatment of even this model is difficult, the following simplifying assumptions are made: (1) the ions continue to move with their initial acceleration and (2) the image charges in the interaction region walls are neglected. It may be shown that, for the dimensions of interest, the initial longitudinal space-charge field is given approximately by

$$E_Z = 8\rho_0 Z_0 \tan^{-1}(w/a), \qquad (23)$$

where ρ_0 is the initial ion space-charge density, Z_0 is the initial coordinate of the particle that experiences the field E_Z, w is the thickness of the cloud, and a is the height of the cloud (Fig. 25). Under the assumption that the ions move with their initial acceleration, the trajectories of the ions are given by

$$Z = Z_0[1 + (t^2/T^2)], \qquad (24)$$

where Z_0 is the initial Z coordinate of an ion, t is measured from the beginning of the explosion, and T is given by

$$T = \left(4\frac{e}{M}\rho_0 \tan^{-1}\frac{w}{a}\right)^{-\frac{1}{2}}, \qquad (25)$$

where ρ_0, w, and a are defined above and e/M is the charge to mass ratio of the ion. The velocity of the ions resulting from the space charge explosion is

$$\dot{Z} = 2Z_0 t/T^2, \qquad (26)$$

where Z_0, t and T are defined above. [The mean velocity used in the section on gas quenching was obtained by evaluating Eq. (26) at a time corresponding to the middle of the rf pulse and at a position corresponding to the center of each of the exploding segments.] Under the above conditions, the ion cloud expands in such a manner that the charge density decreases uniformly:

$$\rho(t) = \rho_0[1 + (t/T)^2]^{-1}, \qquad (27)$$

where $\rho(t)$ is the charge density at the time (t) and ρ_0, t and T are defined above. In computing ρ_0, it is necessary to include the contribution from both ground-state

[39] Novick, Lipworth, and Yergin, Phys. Rev. **99**, 612(A) (1955). The difference between the present theoretical value of S and the value quoted in the above paper results from a small numerical error in the latter value.

[40] *Note added in proof.*—Professor Salpeter has kindly informed us of a small numerical error in the coefficient of the finite mass term. The corrected value of this term is $+2.8$ Mc/sec. The corrected value of S_T is $14\,043.0 \pm 3.0$ Mc/sec.
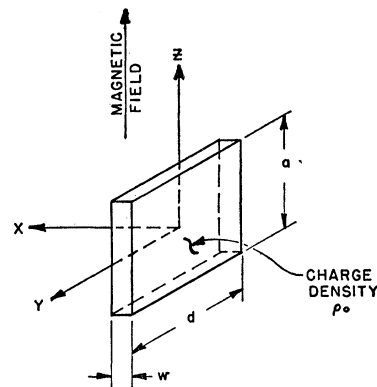

FIG. 25. Space-charge model and coordinate system used for discussing the space-charge explosion.

and metastable ions. Lamb and Skinner estimate that one hundred ground-state ions are formed for every metastable ion (He I, p. 549). The initial charge density is given by

$$\rho_0 = n^0[\sigma^+(1s) + \sigma^+(2s)]J^-T_1, \qquad (28)$$

where n^0 is the gas density, $\sigma^+(1s)$ is the ionization cross section, $\sigma^+(2s)$ is the cross section for excitation to the metastable state of the ion, J^- is the electron beam current density and T_1 is the length of the gun pulse. Typical values for the constants appearing in Eqs. (23)–(28) are:

$$n^0 = 0.748 \times 10^{14} \text{ atom/cc},$$

$$\sigma^+(1s) = 0.37\pi a_0{}^2 \text{ (He I, p. 549)},$$

$$\sigma^+(2s) = 0.37 \times 10^{-2}\pi a_0{}^2 \text{ (He I, p. 549)},$$

$$J^- = 8.40 \times 10^7 \text{ esu/cm}^2/\text{sec},$$

$$T_1 = 0.81 \times 10^{-6} \text{ sec},$$

$$a = 0.865 \text{ cm}, \quad w = 0.0254 \text{ cm},$$

and

$$e/M = 7.227 \times 10^{13} \text{ esu/g}.$$

The corresponding values for ρ_0 and T are

$$\rho_0 = 0.165 \text{ esu/cc}, \quad T = 0.846 \text{ microsecond}. \qquad (29)$$

Thus, in the above model, the ion density drops to one half of its initial value in 0.846 microsecond. The maximum value of the longitudinal electric field acting on those ions exposed to the detector is (see Sec. E1c)

$$E_{z \text{ max}} = 8\rho_0(a/4) \tan^{-1}(w/a) = 2.52 \text{ v/cm}. \qquad (30)$$

Estimates have been made of the errors introduced by the above approximations. It has been found that, if allowance is made for the change in acceleration, the effective value of T, the ion explosion time, is increased by about ten percent. Inclusion of the first twenty images similarly increases T by about 10%. Thus as a result of these two approximations the apparent explosion rate is about twenty percent too fast. No estimate has been made of the effect of the initial thermal and recoil velocities, but it is expected that these initial velocities will hasten the dispersal of the ion cloud.

For the purpose of discussing the transverse ion motion, the longitudinal motion will be ignored. Since the resulting transverse motion is slow compared with the explosion, this procedure leads to an overestimate of the transverse motion. As in the case of the explosion, the initial velocities of the particles will be neglected. If it is further assumed that the ion cloud is of infinite extent in the Y-Z plane (Fig. 25) then the motion is of a particularly simple form. In this case the electric field is a constant of the motion and each particle moves in constant, crossed electric and magnetic fields. The electric field is of course different for particles having different initial X coordinates (Fig. 25). Under these conditions the particle trajectories are cycloids, the

average drift velocity of an ion across the field is

$$\bar{v}_y = cE_x/H, \qquad (31)$$

where c is the velocity of light, H is the magnetic field, and E_x is given by

$$E_x = 4\pi\rho_0 X_0, \qquad (32)$$

where ρ_0 is the initial ion density, and X_0 is the initial X coordinate of the ion (Fig. 25). The maximum value of this transverse field occurs at the edge of the cloud (see Sec. E1c)

$$E_{x \text{ max}} = 4\pi\rho_0 w/2 = 7.90 \text{ v/cm}. \qquad (33)$$

Since the transverse drift velocity of each layer of ions is proportional to the initial displacement of the layer from the center of the cloud, the various layers slip past each other and the cloud undergoes a shearing distortion, the shear axis being parallel to the Y axis (Fig. 25). If the cloud is truly of infinite extent in the Y-Z plane (Fig. 25) and if two conducting sheets are placed parallel to the broad faces of the cloud then there is no change in the above description of the motion. If, however, account is taken of the finite extent of the cloud and its asymmetrical location between the broad faces of the interaction regions, then it is found that the plane of zero slip moves from the center of the cloud to a point about $W/10$ from the center toward the remote wall of the interaction region. Thus there is a net transport of about twenty percent of the cloud along the Y axis (Fig. 25), since this is also the direction of rf propagation this effect leads to a slight Doppler shift.

If the ion cloud extended well beyong the edges of the detection window in the Y direction then the transverse motion would not lead to any net loss of ions; in the actual apparatus at least one edge of the ion cloud is close to the edge of the detection window, this asymmetry results from an asymmetrical electron gun filament temperature distribution. For the purpose of obtaining an upper bound to the ion loss resulting from this transverse motion, it is assumed that both ends of the ion cloud coincide exactly with the edges of the detector window, and it is also assumed that the motion of the ions near the ends of the cloud is the same as it would be for a cloud of infinite extent. Under these conditions the number of ions exposed to the detector is given by

$$N = N_0[1 - \pi(\rho_0 cwt/Hd)], \qquad (34)$$

where N_0 is the number of particles in the field of view at the end of the gun pulse, H is the magnet field, d is the length of the detection window, ρ_0 is the charge density, w is the wdith of the cloud, and t is the time measured from the end of the gun pulse. Taking $d = 0.953$ cm, $w = 0.025$ cm, $\rho_0 = 0.165$ esu/cc, and $H = 7600$ gauss, it is found that the number of particles exposed to the detector dropes to half of the initial value in 8.8 microseconds.

10

APPENDIX II. FIELD DEPENDENCE OF SPACE-CHARGE REMOVAL PROCESSES

The dependence of the ion explosion time (T) upon the ion charge density and the dimensions of the ion cloud is given by Eq. (25). The ratio of the cloud width (w) to height (a) is about 1/34, thus Eq. (25) may be expanded in power of (w/a). It is also convenient to express the charge density in terms of the total charge in the ion cloud (Q_0). Thus Eq. (25) may be rewritten as

$$T=\left(4\frac{e}{M}\frac{Q_0}{a^2d}\right)^{-\frac{1}{2}}\left(1+\frac{1}{6}\frac{w^2}{a^2}\right),\qquad(35)$$

where Q_0 is the total initial charge in the cloud, and w, a, and d are the thickness, height, and depth of the cloud (Fig. 25). Since the electron collector current is held constant as the magnetic field is varied any field dependence in Q_0 must arise from field dependent changes in either the ionization efficiency or the electron collection efficiency. There are good theoretical reasons for believing that the ionization and excitation cross sections are field independent. Since the bombarding electrons follow helical paths and since the diameter of the helices depend upon the magnetic field it might be expected that the ionization efficiency depends upon the magnetic field; however, since the electron spiralling frequency (cyclotron frequency) increases at the same rate as the helix diameter decreases the rectified electron path length is independent of field. Therefore the ionization efficiency is believed to be field independent. The bombarding electrons pass through a double grid system in going from the interaction region to the collection plate. Since the diameters of the electron helices are inversely proportional to the field, there is a small field dependence in the grid transmission factor and in the electron collection efficiency. A larger fraction of the electrons passes through the grid system at high fields than at low fields. The change in grid transmission has been estimated by assuming that the effective size of the grid wires is equal to the geometrical wire diameter plus one electron helix diameter, the helix diameter being computed from the transverse thermal velocity of the electrons. The grid transmission increases by

about 0.067% as the field is varied from the low-field working point to the high-field working point. The correction to S resulting from this effect is $+0.02$ Mc/sec.[41]

As a result of the transverse cycloidal motion the width of the cloud (w) depends slightly upon the magnetic field; at high fields the cloud width is less than at low fields. For the purpose of estimating a correction to S it is assumed that w is inversely proportional to the field. With this assumption the explosion time (T) changes by about 0.0025% between the two working point fields. The corresponding correction to S is -0.002 Mc/sec. The quenching function given by Eq. (19) was used for the evaluation of the above space charge corrections, the gas quenching processes were neglected in this calculation.

In estimating the correction to S resulting from the field dependence of the transverse ion motion, the explosive motion of the ions is ignored. In this manner an upper bound to the correction is obtained. For the purpose of evaluating this correction, a quenching function has been developed which is based on the ion loss function given by Eq. (34). This quenching function is

$$\phi(\mu)=N_0\left\{\left(1-\frac{T_2}{\tau}-\frac{1}{\mu\tau}\right)(1-e^{-\mu T_3})+\frac{T_3}{\tau}e^{-\mu T_3}\right\},\quad(36)$$

where N_0 is the number of metastable ions in the interaction region at the end of the gun pulse, μ is the quenching amplitude given by Eq. (6), T_3 is the length of the rf pulse, T_2 is the delay between the end of the gun pulse and the beginning of the rf pulse and the removal time τ is given by

$$\tau=Hd/\pi\rho_0cw,\qquad(37)$$

where H is the magnetic field, ρ_0 is the ion charge density, and d and w are the depth and width of the ion cloud respectively (Fig. 25). The field dependence of the removal time τ shifts the center of the resonance, as determined at the working point fields, by 0.21 Mc/sec.

---

[41] The principal effect on S arising from the variation in collection efficiency is due to its effect on T [Eq. (35)]. The normalization procedure eliminates the other effects which the variation would have.